9 SIMULATION RESULTS, ANALYSIS AND VALIDATION

9.1 Introduction

In this chapter the simulation results are produced to analyse and validate the IR signature of the scene, the IR seeker missile-target engagement sequences and the expendable IR flare model. The results are produced in numerical data form, 2D and 3D plots and virtual reality scenes. Four test scenarios are shown. The first scenario models a scene comprising of five point source targets at different distances from the detector and calculates the radiance of each target, the transmission of the atmosphere and then the total power received at the detector for estimation of the lock-on range. This analysis is done in a static mode on 2D images. The second scenario takes a target aircraft as a set of sub-targets for high-fidelity modelling and discusses the appearance of the target sub-parts in the IR waveband as per the radiometric properties. The special effects such as leading-edge reflections, exhaust-gas plume and cold-sky reflections from the glass canopy are analysed in the 2D static mode. The third scenario simulates the missile-target engagement sequences and analyses the missile LATAX, different tracking algorithms and hit-criterion. The fourth test scenario simulates the IRCM flare and analyses the spectral and temporal responses and the affects of the physical properties of the flare on its trajectory.

9.2 System Requirements

To run the IR signature modelling and simulation software, the following hardware and software specifications are required.

9.2.1 Hardware Requirements

The model could run on a standard PC (a Pentium III or above) with OpenGL compatible graphics accelerator. However, the machine on which these simulations are run is a DELL Optiplex GX270, 2.80 GHz Intel Pentium IV CPU with 512 MB of RAM and Dell Extreme graphics.

9.2.2 Software Requirements

The software requirements are Microsoft® Windows NT/2000/XP, MathWorks MATLAB® with Virtual Reality Toolbox, OpenGL® with GLUT and Microsoft® Excel. The software versions used are Windows XP Professional (version-5.1, service pack-2), MATLAB (version-7.1.0.246, release-14, service pack-3), Virtual Reality Toolbox (version-4.2.1, release-14, service pack-3) and Excel-2002 (service pack-3).

9.2.3 Software Control

The MATLAB and VRML source codes are kept modular for easy debugging and future upgrades. Records of all the changes made to the algorithms during the development phases have been kept. The m-files of the MATLAB programme and the VRML files of the Virtual world are named as per the date and with a version number to track the changes at any time in the future. The input data, atmospheric transmission data and sky radiance data are stored in the Excel spreadsheets. For backup storage and redundancy all MATLAB m-files, VRML files and the Excel spreadsheets are stored in two separate PCs and also on the Cranfield University central storage facility. Also, as a backup all these files are copied regularly on CDs.

9.3 Presenting Simulation Results

Depending upon the application, the outputs of the simulation could be available in the form of numerical listings or plotted graphically or viewed in 3D virtual reality. The missile-target engagement and countermeasure simulation contains information about the IR signatures of the scene, the dynamic missile fly-out data, countermeasure flare deployment and provides the missile miss-distance and lock-on range. The following paragraphs explain the different ways in which the simulation results are presented. Each method has its own advantages and disadvantages.

9.3.1 Numerical Data

From a computational point of view, the numerical data is the easiest to generate but the most difficult to visualize by humans. However, depending upon the intended application, the numerical data may be useful for some subsequent scientific or mathematical calculations. In this work, the radiance of the targets and the background, the power received at the detector and the lock-on ranges etc. are presented in numerical data form.

9.3.2 Graphical Representation

The second way is to convert the numerical data into graphs. This representation is easier to understand and gives a better understanding of the results for analysis or comparison. The outputs such as the lock-on range, miss-distance, flare temporal response and atmospheric transmission etc. are plotted in 2D graphs. The targets, missile and flare locations and trajectories etc. are shown in 2D and 3D graphs. Also, the radiance and power received at the detector to represent the detector outputs are shown as 2D static images.

9.3.3 3D Virtual Reality

The third approach is to represent the output IR scene in form of 3D virtual reality. This gives a more realistic picture of the outputs and is easy to understand by a human as this gives visual effects. Although, virtual reality is the most convenient way from an understanding point of view, however, from the computational side, it is the most expensive on memory and processing time and needs high processing speed. However, with advancements in the computer technologies and the availability of better 3D computer graphics hardware and software, it is now possible to render 3D virtual reality scenes even on PCs. The MATLAB Virtual Reality Toolbox uses VRML for developing virtual worlds. The 3D visualization of the IR signature scene is done by developing the missile, target, background and flares models in VRML and controlling the movement and appearances of these with algorithms developed in MATLAB as per the IR spectral, temporal and spatial variations.

9.4 Modelling and Simulation Steps

In Chapter 6 to 9, the different steps involved in the modelling of the IR signature scene and simulation of the missile-target engagement are discussed in detail. The typical modelling and simulation steps are summarized as follows:

(a) **Target model.** Selecting the target data from the look up tables. The number of targets, their geometry, location, speed, heading and thermal properties.

(b) **Background model.** Modelling the background scene geometry and its thermal properties.

(c) **Missile model.** Selecting the missile data from the lookup tables. The type of missile, seeker properties, spectral band, location, speed and direction.

(d) **Tracking method.** Selecting the missile tracking method.

(e) **Mode-of-operation**. Selecting the mode-of-operation out of the following: Air-to-air mode, Air-to-ground mode, Surface-to-surface mode and Surface-to-air mode. At this moment, only air-to-air and surface-to-air modes are modelled.

(f) **Flare Model.** Selecting the flare input data from the lookup tables. The number of flares, thermal properties and their dispensation sequences.

(g) **Environmental Model.** The environmental conditions such as the type of atmosphere, weather conditions and altitude.

(h) **Initial Conditions and Assumptions.** To start the simulation by selecting the initial conditions and the assumptions made for the targets, the missile and the flares.

(i) **Target Manoeuvres.** Selecting the target aircraft manoeuvre and the mode of operation.

(j) **Scenario Build-up.** To run a specific missile-target engagement sequence, the targets and missile are located at relative positions in the world coordinates and the timings of the countermeasures dispensation are planned accordingly.

(k) **Running simulations.** The simulation is run as per the setup and the results are recorded in the form of numerical data, plots, images and virtual reality animations.

9.5 Explanation of the Test Scenario No. 1

To generate a set of results for 2D static IR signature analysis, a scenario of five point targets at different distances from the seeker is considered. The following paragraphs explain the inputs, setup and the outputs for this test scenario. The radiance of the targets and the background is calculated, the atmospheric transmission is calculated for the distance between the seeker and the targets and the power received at the detector is calculated and the lock-on range is estimated.

9.5.1 Input Data for Test Scenario No. 1

The various inputs fed in to build the Test Scenario No. 1 are as under:

9.5.1.1 Mode of Operation

The mode of operation is kept as "air-to-air". This is used in LOWTRAN for calculating the transmission data sets.

9.5.1.2 Missile Parameters

Type of Missile	:	Air-to-Air
Noise Equivalent Power (*NEP*)	:	10^{-10} W/Hz$^{1/2}$
Signal-to-noise-ratio (*SNR*)	:	2
Optics Diameter	:	60.00 mm
Seeker field-of-view	:	2^{o}
Optics Transmission	:	0.7
Detector Size	:	0.1 mm
Pixel Image Size	:	512 x 512 pixels
Spectral Band coverage	:	8 to 12 μm

Note: These values are taken as an example and do not represent any actual missile system.

9.5.1.3 Atmospheric Parameters

The atmospheric parameters are selected on the basis of three weather conditions such as: "*good*", "*typical*" and "*bad*". The three weather conditions are explained in Chapter-6 Table 6-4.

9.5.1.4 Background Parameters

Type of background	:	Sky
Type of Sky	:	Clear
Altitude	:	1000 meters
Distance from seeker	:	6 km

9.5.1.5 Target Input Parameters

Number of Targets	I	II	III	IV	V
Emissivity	0.95	0.8	0.98	0.95	0.8
Temperature (K)	400	600	900	400	600
Area (m^2)	20	120	50	20	120
Range from seeker (km)	1	5	3	6	2

9.5.1.6 Entering Targets Locations

The targets locations are entered by clicking the mouse within the FOV window as shown in Figure 9-1.

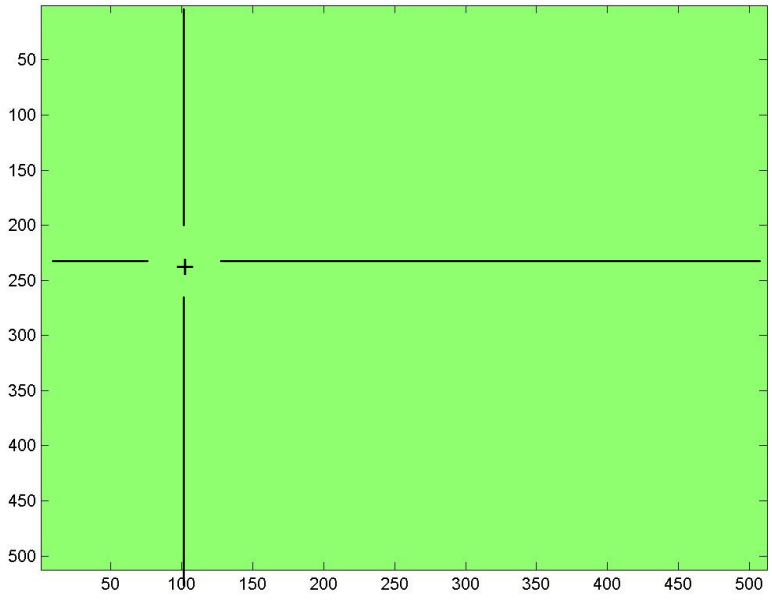

Figure 9-1: Window for entering targets locations

9.5.2 Results of Test Scenario No. 1

The outputs of the Test Scenario No. 1 are taken in the form of the numerical values based on the calculations, the graphs and the 2D images of the IR signatures of the scene.

9.5.2.1 Numerical Results

To develop the IR signature scene model and to calculate the lock-on range, the projected area, target area, background area, the radiances, the power per unit area and

the total power received at the detector are calculated. The numerical results for the "*good*", "*typical*" and "*bad*" weather conditions are tabulated in Table 9-1, Table 9-2 and Table 9-3 respectively.

Table 9-1: Numerical results of Test Scenario No. 1 for "good" weather

VARIABLE	UNITS	I	II	III	IV	V
Projected Area	m^2	3.6 $x10^5$				
Background Total Radiance	W m^{-2} sr^{-1}	0.2798				
Background Total Radiance after Attenuation	W m^{-2} sr^{-1}	0.1971				
Background Power per Unit Area	W m^{-2}	1.0837 $x10^{-11}$				
Background Area	m^2	3.5781 $x10^5$				
Solid-angle Background	Radian	7.854 $x10^{-11}$				
Background Total Power	W	3.8776 $x10^{-6}$				
Target Exposed Area	m^2	0.7200 $x10^3$	0.1728 $x10^3$	0.2000 $x10^3$	0.0200 $x10^3$	1.0800 $x10^3$
Target Total Radiance	W m^{-2} sr^{-1}	126.8	395.6	1270.0	126.8	395.6
Target Total Radiance after Attenuation	W m^{-2} sr^{-1}	118.6	282.8	1024.0	87.1	343.7
Target Power per Unit Area	W m^{-2}	0.2347 $x10^{-6}$	0.0224 $x10^{-6}$	0.2252 $x10^{-6}$	0.0048 $x10^{-6}$	0.1701 $x10^{-6}$
Solid-angle Target	Radian	0.2827 $x10^{-8}$	0.0113 $x10^{-8}$	0.0314 $x10^{-8}$	0.0079 $x10^{-8}$	0.0707 $x10^{-8}$
Target Total Power	W	0.0469 $x10^{-4}$	0.0269 $x10^{-4}$	0.1126 $x10^{-4}$	0.0010 $x10^{-4}$	0.2041 $x10^{-4}$
Lock-on Range	km	41.53	70.56	73.72	41.53	70.56
Target Exposed Area	in pixels	529	121	144	16	784
Target Location	row column	100 100	200 150	250 250	300 300	400 350

Table 9-2: Numerical results of Test Scenario No. 1 for "typical" weather

VARIABLE	UNITS	I	II	III	IV	V
Projected Area	m^2	3.6 $x10^5$				
Background Total Radiance	W m^{-2} sr^{-1}	0.2798				
Background Total Radiance after Attenuation	W m^{-2} sr^{-1}	0.1145				
Background Power per Unit Area	W m^{-2}	6.2947 $x10^{-12}$				
Background Area	m^2	3.5781 $x10^5$				
Solid-angle Background	Radian	7.854 $x10^{-11}$				
Background Total Power	W	2.2523 $x10^{-6}$				
Target Exposed Area	m^2	0.7200 $x10^3$	0.1728 $x10^3$	0.2000 $x10^3$	0.0200 $x10^3$	1.0800 $x10^3$
Target Total Radiance	W m^{-2} sr^{-1}	126.8	395.6	1270	126.8	395.6
Target Total Radiance after Attenuation	W m^{-2} sr^{-1}	107.91	176.41	767.75	49.99	283.93
Target Power per Unit Area	W m^{-2}	0.2136 $x10^{-6}$	0.0140 $x10^{-6}$	0.1688 $x10^{-6}$	0.0027 $x10^{-6}$	0.1405 $x10^{-6}$
Solid-angle Target	Radian	0.2827 $x10^{-8}$	0.0113 $x10^{-8}$	0.0314 $x10^{-8}$	0.0079 $x10^{-8}$	0.0707 $x10^{-8}$
Target Total Power	W	0.0427 $x10^{-4}$	0.0168 $x10^{-4}$	0.0844 $x10^{-4}$	0.0005 $x10^{-4}$	0.1686 $x10^{-4}$
Lock-on Range	km	23.99	37.08	38.46	23.99	37.08
Target Exposed Area	in pixels	529	121	144	16	784
Target Location	row column	100 100	200 150	250 250	300 300	400 350

Table 9-3: Numerical results Test Scenario No. 1 for "bad" weather

VARIABLE	UNITS	I	II	III	IV	V
Projected Area	m^2	3.6 $x10^5$				
Background Total Radiance	W m^{-2} sr^{-1}	0.2798				
Background Total Radiance after Attenuation	W m^{-2} sr^{-1}	0.0021				
Background Power per Unit Area	W m^{-2}	1.1422 $x10^{-13}$				
Background Area	m^2	3.5781 $x10^5$				
Solid-angle Background	Radian	7.854 $x10^{-11}$				
Background Total Power	W	4.0868 $x10^{-8}$				
Target Exposed Area	m^2	0.7200 $x10^3$	0.1728 $x10^3$	0.2000 $x10^3$	0.0200 $x10^3$	1.0800 $x10^3$
Target Total Radiance	W m^{-2} sr^{-1}	126.8	395.6	1270	126.8	395.6
Target Total Radiance after Attenuation	W m^{-2} sr^{-1}	55.04	6.28	102.84	0.9162	74.09
Target Power per Unit Area	W m^{-2}	0.1089 $x10^{-6}$	0.0005 $x10^{-6}$	0.0226 $x10^{-6}$	0.0001 $x10^{-6}$	0.0367 $x10^{-6}$
Solid-angle Target	Radian	0.2827 $x10^{-8}$	0.0113 $x10^{-8}$	0.0314 $x10^{-8}$	0.0079 $x10^{-8}$	0.0707 $x10^{-8}$
Target Total Power	W	0.2179 $x10^{-5}$	0.0060 $x10^{-5}$	0.1131 $x10^{-5}$	0.0001 $x10^{-5}$	0.4399 $x10^{-5}$
Lock-on Range	km	7.36	10.11	10.40	7.36	10.11
Target Exposed Area	in pixels	529	121	144	16	784
Target Location	row column	100 100	200 150	250 250	300 300	400 350

9.5.2.2 Output Plots for Test Scenario No. 1

The lock-on ranges calculated for the five targets for different weather conditions is summarized and shown in Figure 9-2 for the "*good*", "*typical*" and "*bad*" weather conditions.

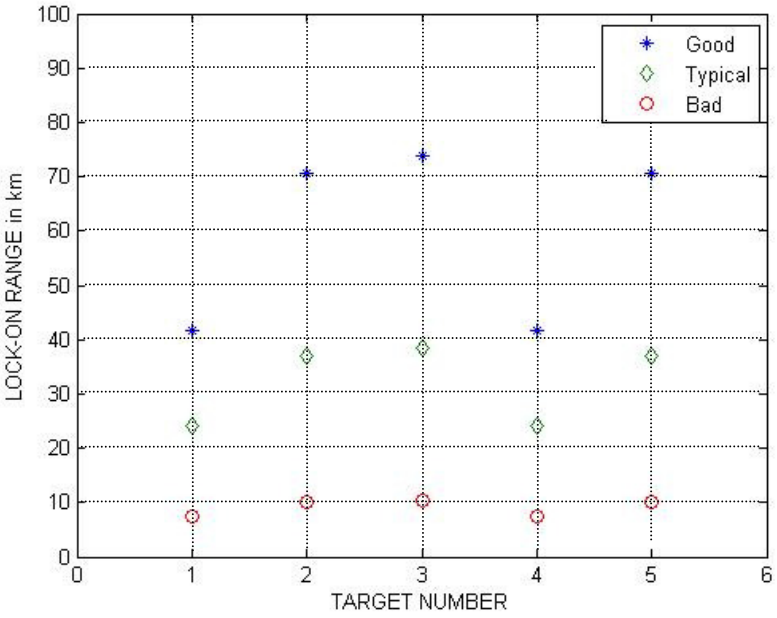

Figure 9-2: Lock-on range of five targets for different weather conditions

The atmospheric transmission for the one kilometre horizontal path length at an altitude of 1000 meters is calculated using the LOWTRAN atmospheric transmission code. Figure 9-3 and Figure 9-4 shows the transmission data for 3-5 micron and 8-12 micron wavebands respectively.

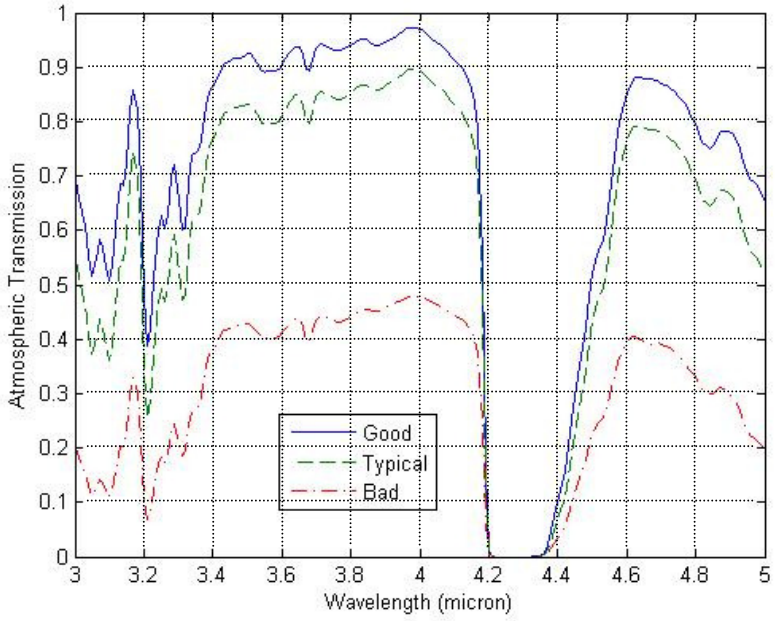

Figure 9-3 : Atmospheric transmission for 3 to 5 micron waveband

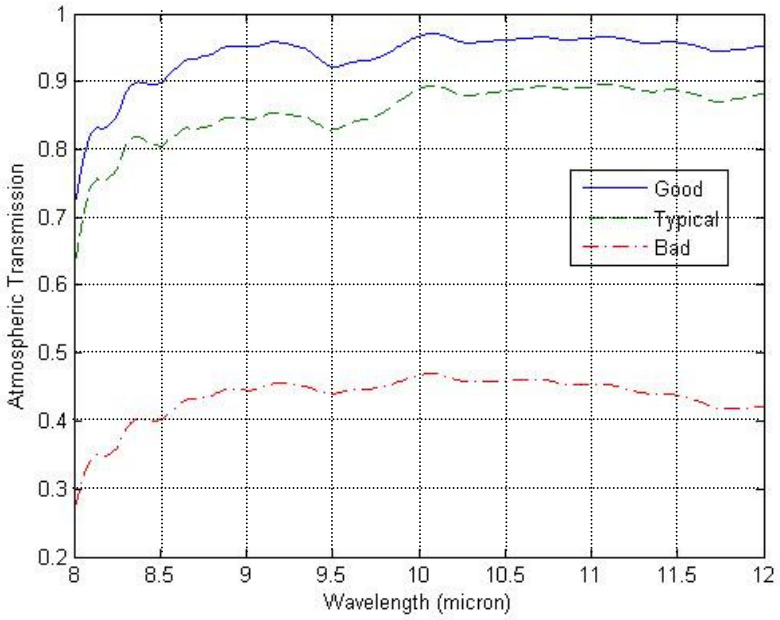

Figure 9-4 : Atmospheric transmission data for 8 to 12 micron waveband

The sky radiance for the horizontal path length of 200 km is calculated using the LOWTRAN atmospheric transmission code. Figure 9-5 shows the sky radiance for the 3 to 5 micron wave band at sea level, 1000 meters and 10 km altitude. Similarly, Figure 9-6 shows the sky radiance for 8 to 12 micron waveband.

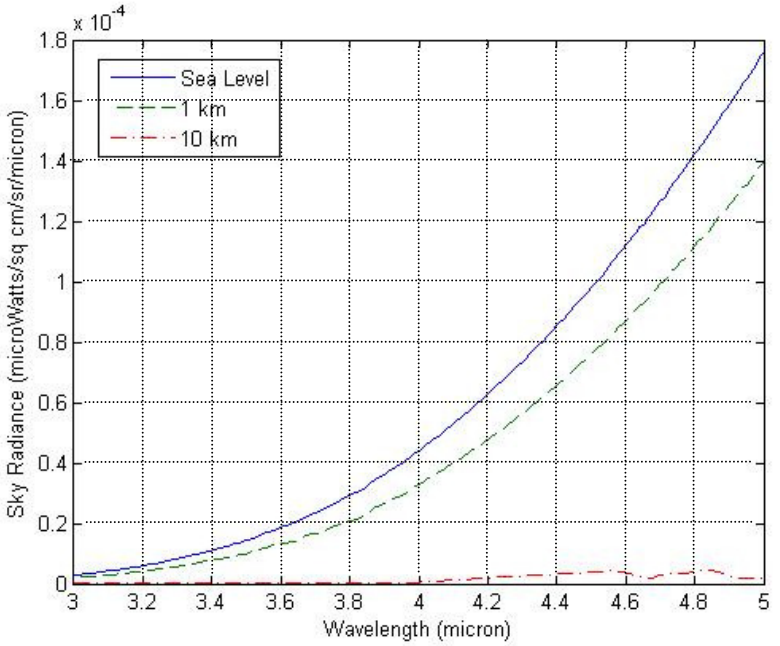

Figure 9-5: Sky radiance for 3 to 5 micron waveband

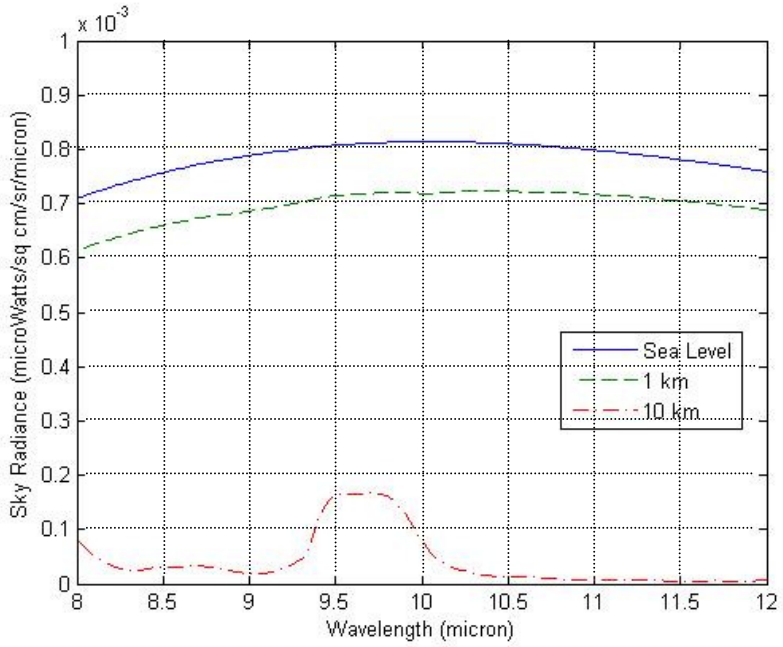

Figure 9-6: Sky radiance for 8 to 12 micron waveband

9.5.2.3 Output Images of Test Scenario No. 1

The three sets of images to represent the IR signature of the scene are generated for the "*good*", "*typical*" and "*bad*" weather conditions. Figure 9-7 shows the images for the "*good*" weather. The image contains five targets at different ranges and of different projected areas. The details of these targets are given in Table 9-1 on page 214. The targets normalized radiance after atmospheric transmission is shown as per the colour-index given on the side of the image. Similarly, Figure 9-8 and Figure 9-9 shows the images for the "*typical*" and "*bad*" weather conditions respectively.

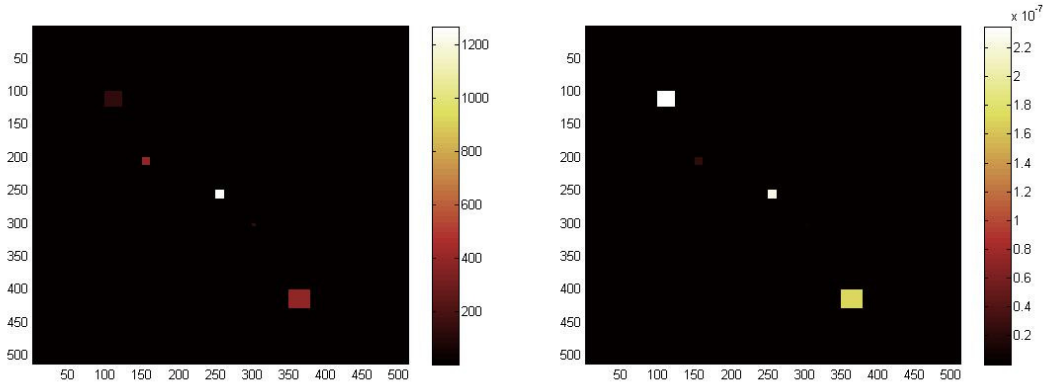

(a) Radiance (b) Power per unit area

Figure 9-7: Image showing 5 targets at different ranges for "good" weather conditions

The first image (a) in all three cases is the scene developed using the radiances of all the targets and the background before the atmospheric attenuation. The second image (b) in all three cases is representing the power per unit area received at the detector from the targets and background after the atmospheric effects. In these images, the area of each target in pixels is shown as per their distance from the detector.

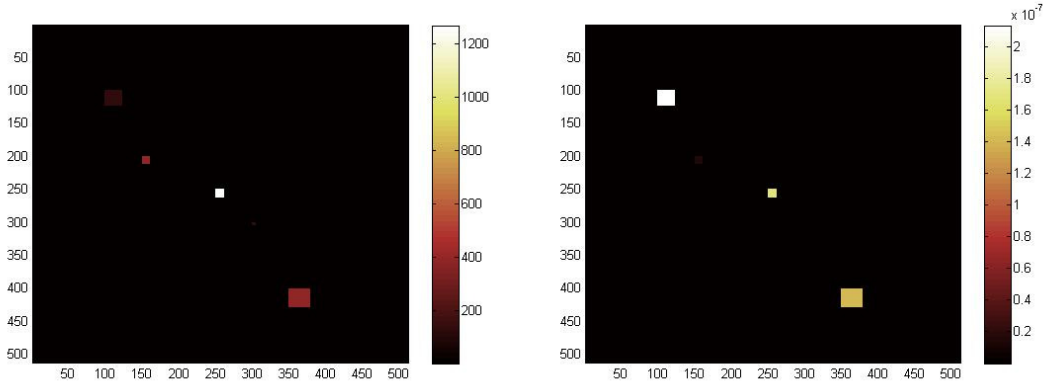

(a) Radiance (b) Power per unit area

Figure 9-8: Image showing 5 targets at different ranges for "typical" weather conditions

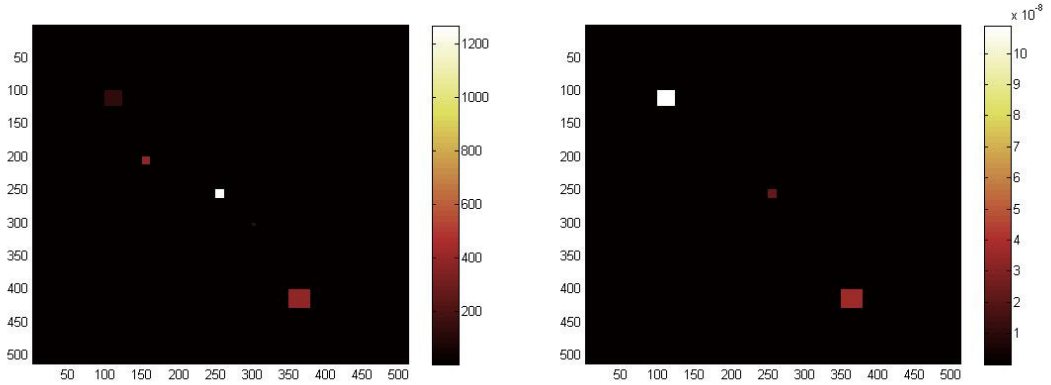

(a) Radiance (b) Power per unit area

Figure 9-9: Image showing 5 targets at different ranges for "bad" weather conditions

9.5.3 Discussion on Results of Test Scenario No. 1

The results of Test Scenario No. 1 are analyzed as under:

(a) The radiance of targets depends upon the temperature, emissivity and the spectral waveband. In Table 9-1 the radiance of target No III is the maximum as its temperature is highest and also the emissivity is more as compared to the other four targets. In Table 9-1, the total radiance of

the target No I and IV are the same, however, target No. I is at a distance of 1 km from the detector whereas, target No. IV is at 6 km, therefore, after atmospheric attenuation the radiance of target No. IV is reduced more as compared to the radiance of the target No. I. Hence with increase in distance the radiance decreases. Comparing the radiance of target No. III after atmospheric attenuation for "*good*", "*typical*" and "*bad*" weather conditions in Table 9-1, Table 9-2 and Table 9-3 respectively, the radiance is decreasing more rapidly as the atmospheric attenuation is getting more. Therefore, the effect of the weather and the distance on the IR radiations is adverse.

(b) The lock-on range of the detector depends upon many factors. The contrast of the target and background radiance, the target cross-sectional area, the detector *NEP* and *SNR*, the optics transmission and diameter are the factors which affect the lock-on range. However, keeping all these factors constant, in Figure 9-2, the lock-on range of all targets has decreased with increase in the atmospheric attenuation. Hence, the atmospheric attenuation adversely affects the lock-on range.

(c) The Sky radiance is dependent on the altitude and the spectral band. In Figure 9-5, for the 3 to 5 micron waveband, the sky radiance is less as compared to the 8 to 12 micron waveband sown in Figure 9-6. In Figure 9-6 the sky radiance for the three different altitudes are plotted. The graph shows that the higher the altitude less is the sky radiance.

(d) The cross-sectional area of the target No. II and V are same, but as target No. II is at a distance of 5 km and the target No. V is at 2 km, therefore, as shown in Figure 9-7(a), the exposed area of target No. II (172.8 m^2) is much less as compared to the exposed area of the target No. V (1080 m^2). Also, as the exposed area of target No. V is more, therefore, the total power received at detector due to target No. V is much more as compared to target No. II. The different power values are visible in the image of Figure 9-7(b).

9.6 Explanation of the Test Scenario No. 2

In the second test scenario the target aircraft is considered as a set of sub-targets for high-fidelity modelling. The appearance of the sub-targets in the IR waveband as per

the radiometric properties is analysed. The leading-edge reflection, the exhaust gas plume, the cold-sky reflections from the canopy are analysed for their appearance in the virtual world. The analysis is done in the static 2D mode. The radiance values are converted into a corresponding RGB colour-map. The IR signature of one static aircraft at 1000 meters altitude is analysed from the seeker of an air-to-air missile at the same altitude, which is 1000 meters. The distance between the target and missile is kept as 750 meters. The IR spectral bands of 3 to 5 and 8 to 12 micron are considered. The missile is viewing the aircraft from the beam, tail and nose aspects.

9.6.1 Input Data for Test Scenario No. 2

The following paragraphs explain the inputs for the Test Scenario No. 2.

9.6.1.1 Mode of Operation

The mode of operation is kept as "air-to-air" for the LOWTRAN data runs.

9.6.1.2 Missile Parameters

Type of Missile	:	Air-to-air
Detector Size	:	0.3 mm
Image Size in pixels	:	256 x 256 pixels
Spectral Band Coverage	:	3 to 5 and 8 to 12 μm
Range between target and missile	:	750 meters

9.6.1.3 Atmospheric Parameters

The atmospheric parameters are selected on the basis of the "*good*" weather conditions as defined in Chapter-6 Table 6-4.

9.6.1.4 Background Parameters

Background upper Hemisphere	:	Three Layers of Sky
Type of Sky	:	Clear
Altitude of layers	:	sea level, 1000 meters, 10 km
Distance from seeker	:	0.75 km
Background lower Hemisphere	:	Ground
Temperature	:	290 K
Emissivity	:	0.9

9.6.1.5 Target Input Parameters

The sub-target temperature, area and radiometric properties are shown in Table 9-4.

Table 9-4 : Target input parameters for test scenario No 2

PART	EMISSIVITY	REFLECTIVITY	TRANSMISSIVITY	TEMPERATURE	AREA
Body	0.9	0.1	0.0	320 K	30 m^2
Nose	0.9	0.1	0.0	350 K	2 m^2
Leading Edges	0.9	0.1	0.0	350 K	1 m^2
Tail pipe	0.9	0.1	0.0	380 K	2 m^2
Canopy	0.5	0.5	0.0	250 K	4 m^2
Plume inner	Spectral	0.0	0.5	1000 K	1 m^2
Plume outer	Spectral	0.0	0.5	500 K	2.5 m^2

The spectral emissivity of the exhaust gas plume is shown in Figure 9-10 for the spectral band of 3.4 to 5 micron. The emissivity of the plume is considered a zero for rest of the spectrum [RIC07].

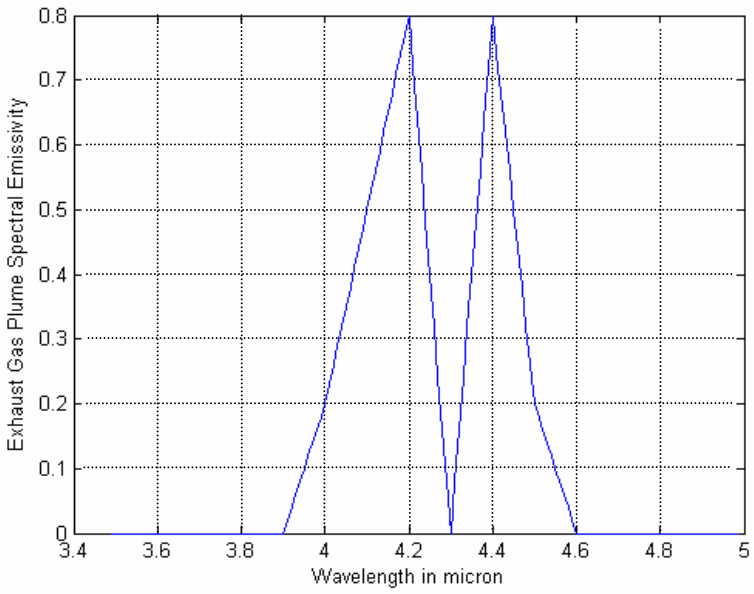

Figure 9-10 : The spectral emissivity of the exhaust gas plume (source [RIC07])

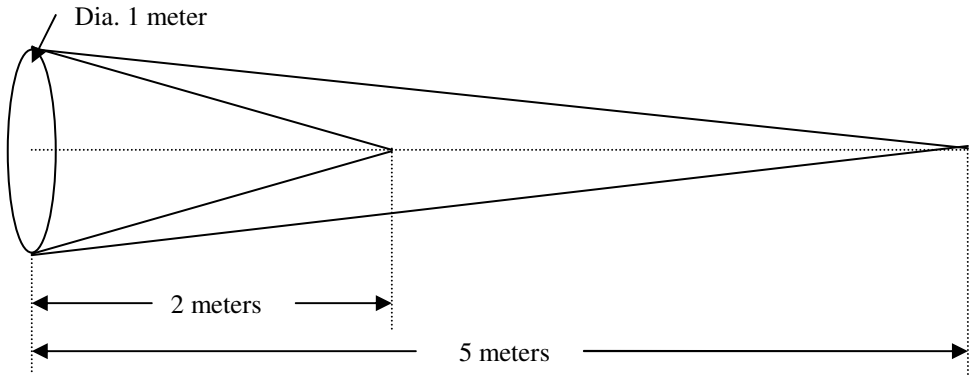

Figure 9-11 : Dimensions of the exhaust gas plume geometry

The inviscid core of the exhaust gas plume is modelled as co-centric cones. The dimensions of the cones are shown in Figure 9-11. The material field values for the sub-targets are shown in Table 9-5.

Table 9-5 : Input material properties of the sub-targets for test scenario No. 2

Sub-Target	Ambient Intensity	Diffuse Color	Emissive Color	Shininess	Specular Color	Transparency
Body	0	0	N_{body}	0	0	0
Nose	0.5	N_{nose}	N_{nose}	0.8	N_{nose}	0
Leading Edges	1.0	N_{edge}	N_{edge}	0.1	N_{edge}	0
Tail-pipe	0	0	$N_{tailpipe}$	0	0	0
Canopy	1.0	0	N_{canopy}	0.7	N_{sky}	0
Exhaust Plume Inner	0	0	N_{plminn}	0	0	0.5
Exhaust Plume Outer	0	0	N_{plmout}	0	0	0.5

NOTE: The diffused colour, emissive colour and specular colour are calculated in RGB colours which correspond to the radiance values of each sub-target.

9.6.2 Results of Test Scenario No. 2

The numerical values of the target and background radiance and the corresponding colour are given in Table 9-6 for the 3 to 5 micron waveband and the values for the 8 to 12 micron waveband are given in Table 9-7. The sub-targets I, II, III, IV and V mentioned in Table 9-6 and Table 9-7 correspond to the "body", "nose", "leading edges", "tail-pipe" and "canopy" respectively.

Table 9-6 : Outputs of test scenario No. 2 for 3 to 5 micron waveband

VARIABLE	UNITS	I	II	III	IV	V
Background Total Radiance	$W\ m^{-2}\ sr^{-1}$	1.1601				
Background Total Radiance after Attenuation	$W\ m^{-2}\ sr^{-1}$	2.1774×10^{-11}				
Sky Total Radiance after Attenuation (three layers)	$W\ m^{-2}\ sr^{-1}$	0.2232×10^{-12}	0.1652×10^{-12}	0.0020×10^{-12}		
Sub-target Total Radiance (five sub-parts)	$W\ m^{-2}\ sr^{-1}$	3.3372	8.0988	8.0988	17.2457	0.1092
Sub-target Total Radiance after Attenuation	$W\ m^{-2}\ sr^{-1}$	0.0701×10^{-9}	0.1845×10^{-9}	0.1845×10^{-9}	0.4171×10^{-9}	0.0016×10^{-9}
Exhaust Gas Plume Total Radiance (two layers)	$W\ m^{-2}\ sr^{-1}$	748.619	24.4882			
Exhaust Gas Plume Radiance after Attenuation	$W\ m^{-2}\ sr^{-1}$	0.2711×10^{-7}	0.0071×10^{-7}			
Maximum Radiance	$W\ m^{-2}\ sr^{-1}$	0.2711×10^{-7}				
Normalizing Factor		$9.4424 \times 10^{+9}$				
Normalized Radiance Background		0.2056				
Normalized Radiance Sky		0.0021	0.0016	0.0000		
Normalized Radiance Sub-target		0.6616	1.7424	1.7424	3.9383	0.0155
Normalized Radiance Exhaust Gas Plume		256	6.7154			
Colour Background (RGB)	Red Green Blue	0 0 0.5156				
Colour Sky	Red Green Blue	0 0 0.5156	0.0 0.0 0.5156	0.0 0.0 0.5156		
Colour Sub-targets	Red Green Blue	0.0 0.0 0.5156	0.0 0.0 0.5315	0.0 0.0 0.5315	0.0 0.0 0.5625	0.0 0.0 0.5156
Colour Exhaust Gas Plume	Red Green Blue	0.5 0.0 0.0	0.0 0.0 0.6094			

Table 9-7 : Outputs of test scenario No. 2 for 8 to 12 micron waveband

VARIABLE	UNITS	I	II	III	IV	V
Background Total Radiance	W m^{-2} sr^{-1}	29.1956				
Background Total Radiance after Attenuation	W m^{-2} sr^{-1}	1.9188 x10^{-10}				
Sky Total Radiance after Attenuation (three layers)	W m^{-2} sr^{-1}	0.2076 x10^{-11}	0.1836 x10^{-11}	0.0126 x10^{-11}		
Sub-target Total Radiance (five sub-parts)	W m^{-2} sr^{-1}	47.0296	70.0883	70.0883	98.4048	7.2604
Sub-target Total Radiance after Attenuation	W m^{-2} sr^{-1}	0.3054 x10^{-9}	0.4496 x10^{-9}	0.4496 x10^{-9}	0.6240 x10^{-9}	0.0484 x10^{-9}
Exhaust Gas Plume Total Radiance (two layers)	W m^{-2} sr^{-1}	0.0	0.0			
Exhaust Gas Plume Total Radiance after Attenuation	W m^{-2} sr^{-1}	0.0	0.0			
Maximum Radiance	W m^{-2} sr^{-1}	0.6240 x10^{-9}				
Normalizing Factor		4.1025 x10^{+11}				
Normalized Radiance Background		78.7174				
Normalized Radiance Sky		0.8517	0.7534	0.0518		
Normalized Radiance Sub-target		125.269	184.447	184.447	256.000	19.8597
Normalized Radiance Exhaust Gas Plume		0.0	0.0			
Colour Background (RGB)	Red Green Blue	0.0 0.7344 1.0000				
Colour Sky	Red Green Blue	0.0 0.0 0.5156	0.0 0.0 0.5156	0.0 0.0 0.5156		
Colour Sub-targets	Red Green Blue	0.4531 1.000 0.5469	1.000 0.6250 0.0	1.000 0.6250 0.0	0.500 0.0 0.0	0.0 0.0 0.8125
Colour Exhaust Gas Plume	Red Green Blue	0.0 0.0 0.5156	0.0 0.0 0.5156			

The output images captured for the 3-5 and 8-12 micron waveband from the beam aspect are shown in Figure 9-12. The nose and tail aspects images are shown in Figure 9-13 and Figure 9-14 respectively.

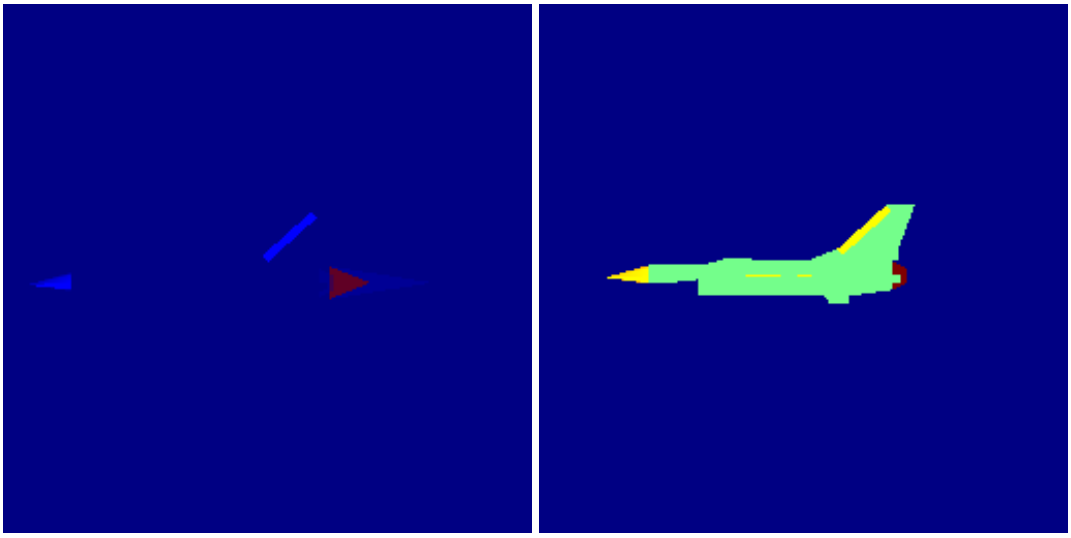

(a) 3 to 5 micron (b) 8 to 12 micron

Figure 9-12 : 256x256 image of target aircraft at 0.75 km range from beam aspect

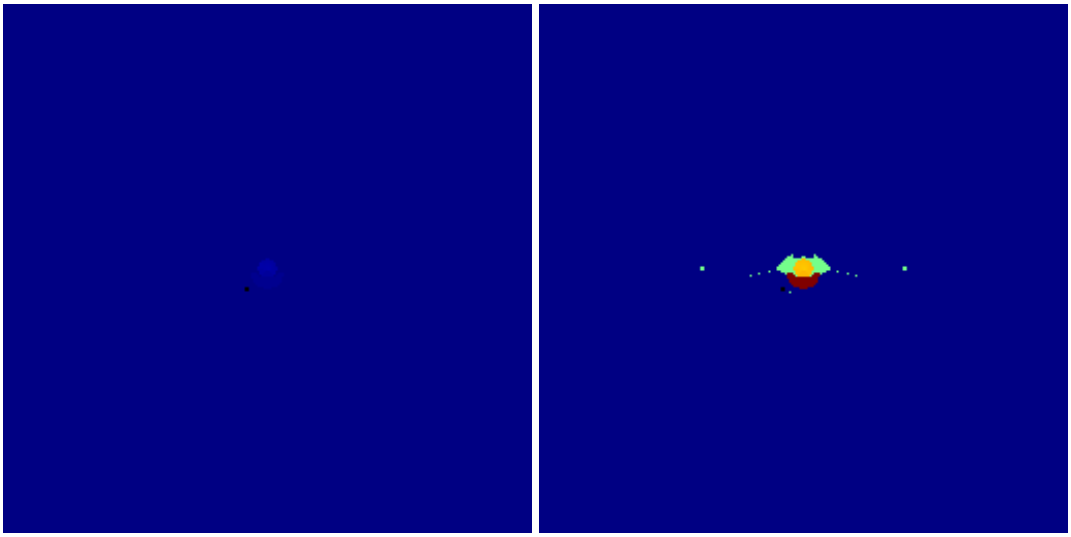

(a) 3 to 5 micron (b) 8 to 12 micron

Figure 9-13 : 256x256 image of target aircraft at 0.75 km range from nose aspect

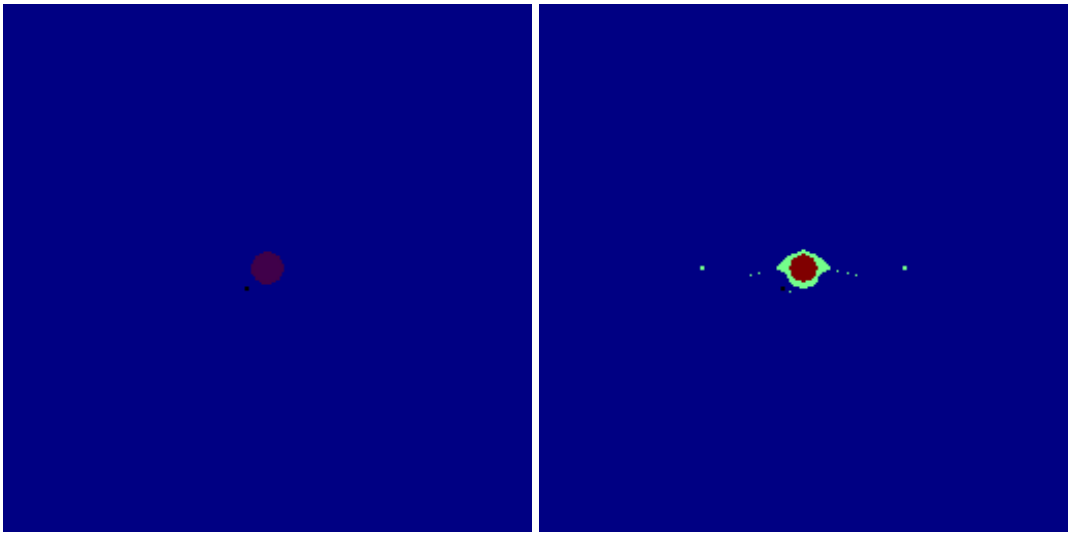

(a) 3 to 5 micron (b) 8 to 12 micron

Figure 9-14 : 256x256 image of target aircraft at 0.75 km range from tail aspect

The same images of Figure 9-12, Figure 9-13 and Figure 9-14 are recaptured without the background and are shown as Figure 9-15, Figure 9-16 and Figure 9-17 respectively.

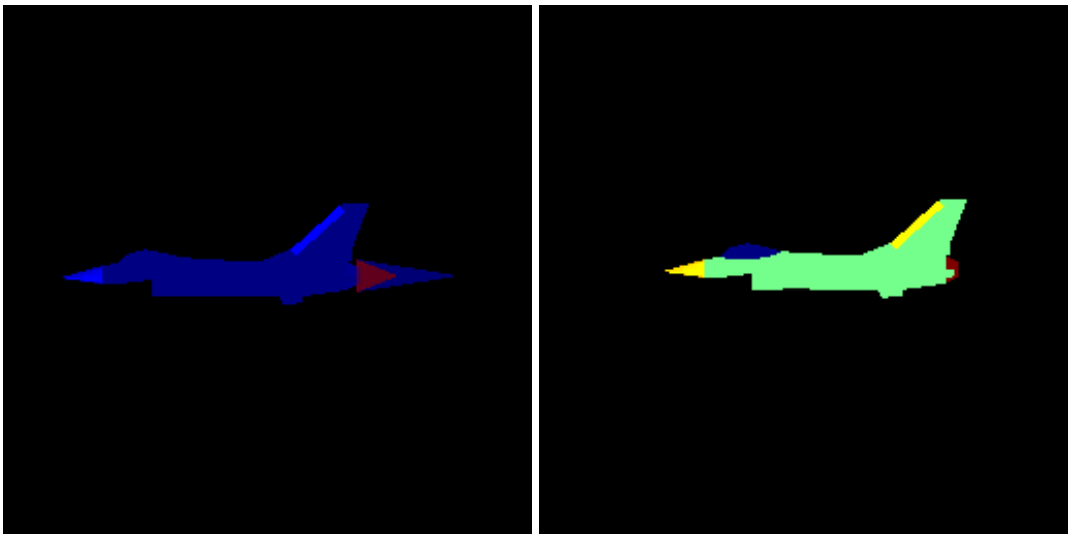

(a) 3 to 5 micron (b) 8 to 12 micron

Figure 9-15 : 256x256 image of target aircraft without background from beam aspect

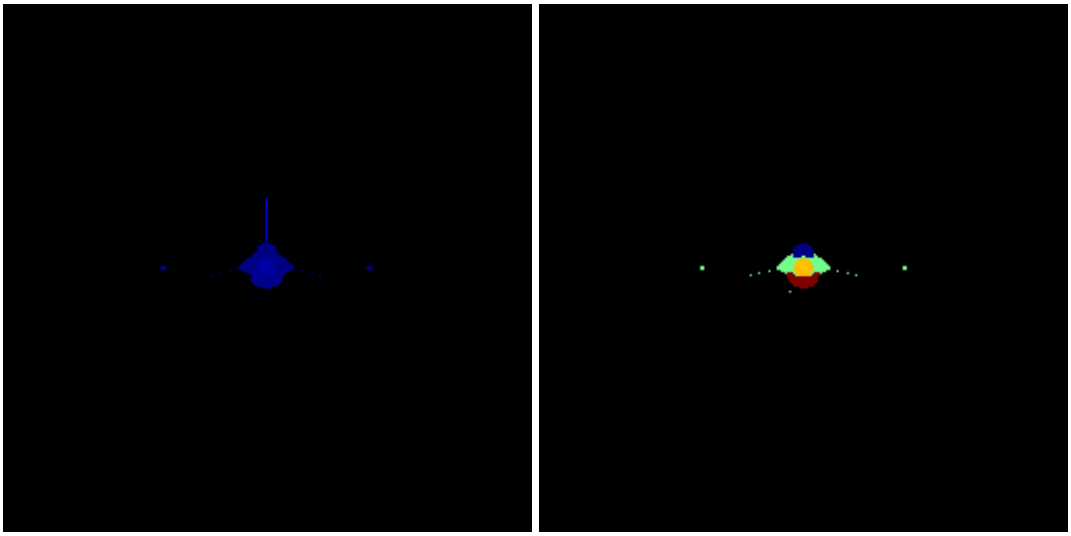

(a) 3 to 5 micron (b) 8 to 12 micron

Figure 9-16 : target aircraft image without background captured from nose aspect

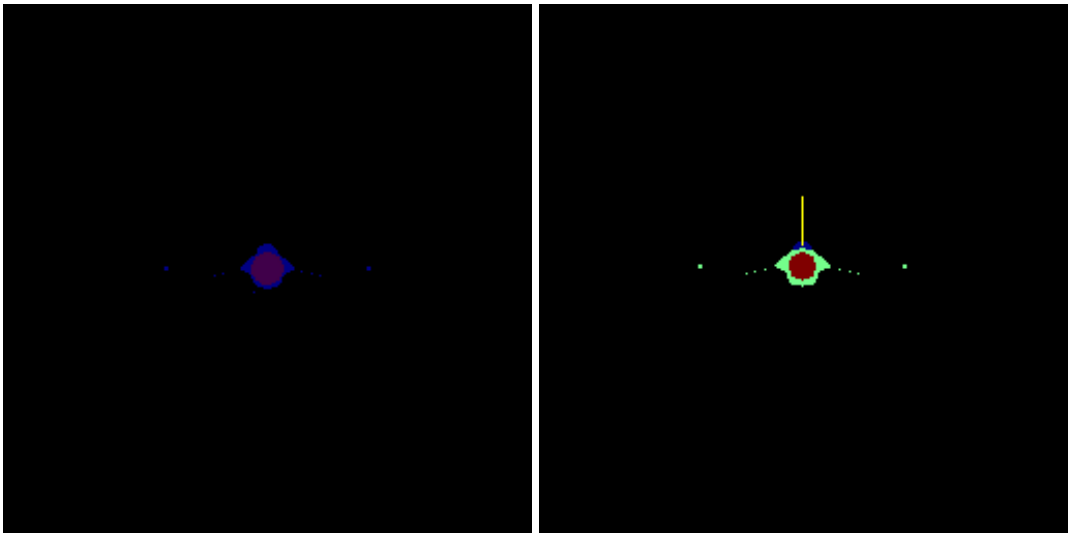

(a) 3 to 5 micron (b) 8 to 12 micron

Figure 9-17 : Target aircraft image without background captured from tail aspect

Figure 9-18 shows the affect of the reflections on the over all IR signatures of the target in 3 to 5 micron waveband. The same is shown in Figure 9-19 without background.

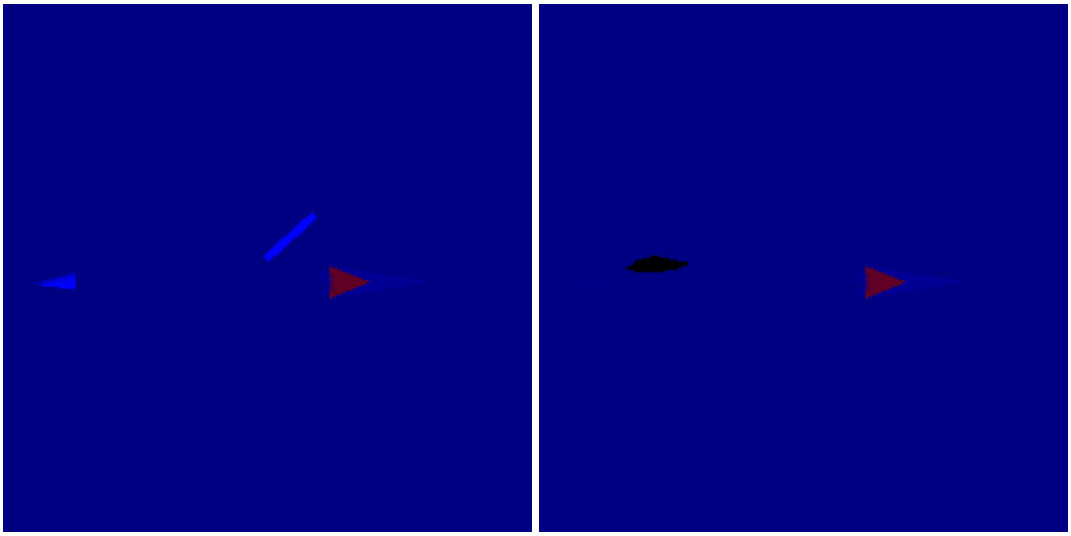

(a) With reflection (b) Without reflection

Figure 9-18 : target image in 3 to 5 micron band with and without reflection effects

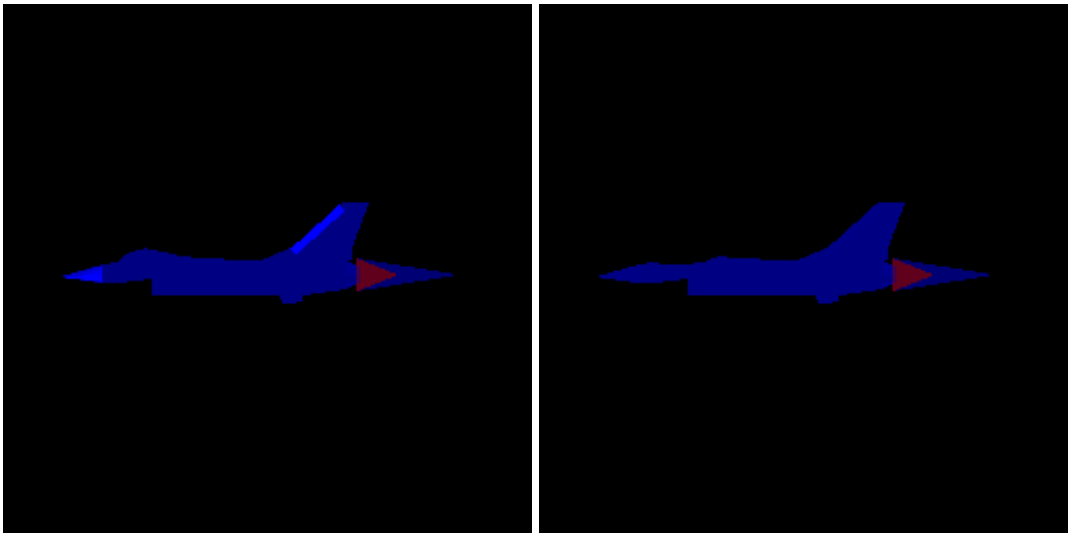

(a) With reflection (b) Without reflection

Figure 9-19 : Target image in 3 to 5 micron band without background

Figure 9-20 shows the reflection effects in 8 to 12 micron waveband. The same image without background are shown in Figure 9-21.

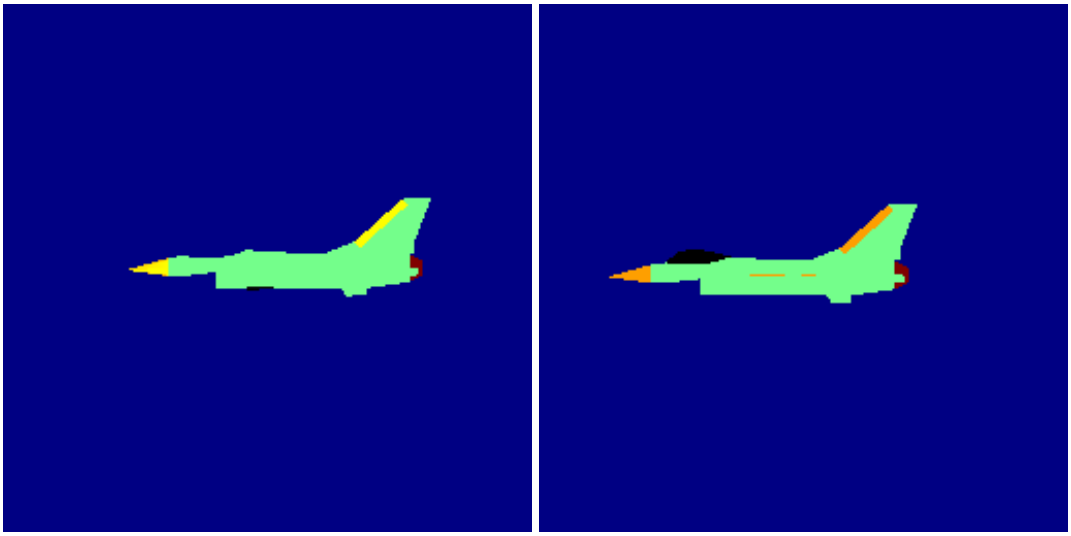

(a) With reflection (b) Without reflection

Figure 9-20 : Target/background image in 8 to 12 micron band showing reflection effects

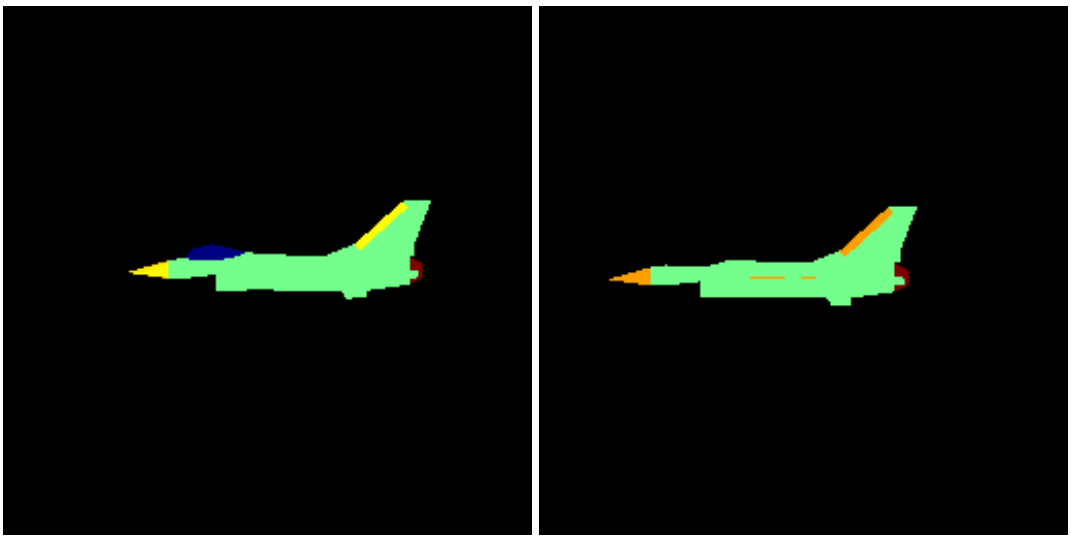

(a) With reflection (b) Without reflection

Figure 9-21 : Target image in 8 to 12 micron band without background

Different colour-maps have been tried to see how they represent the IR signature scene in 3 to 5 and 8 to 12 micron wavebands. The 2D images of the IR scene with these different colour-maps have been observed (these colour-maps are discussed in Chapter-7 paragraph 7-5-2-3) and Table 9-8 summarizes the visual effects.

Table 9-8 : Summary of Colour-map response in 3-5 and 8-12 micron wavebands

COLOR MAP	3-5 MICRON BAND	APPEAR-ANCE	8-12 MICRON BAND	APPEAR-ANCE
HOT	Body : no contrast (OK) Edges : very dim reflection Canopy: no reflection Plume : good contrast	BAD	Body : good contrast Edges : low reflection Canopy: low reflection	BAD
JET	Body : no contrast (OK) Edges : good reflection Canopy: prominent ref Plume : good contrast	GOOD	Body : visible Edges : prominent reflection Canopy: good reflection	GOOD
GRAY	Body : not visible Edges : no reflection Canopy: no reflection Plume : only inner vis	BAD	Body : visible Edges : good reflection Canopy: no reflection	BAD
BONE	Body : not visible Edges : no reflection Canopy: no reflection Plume : only inner vis	BAD	Body : visible Edges : good reflection Canopy: no reflection	BAD
HSV	Body : not visible Edges : no reflection Canopy: good reflection Plume : not good	BAD	Body : visible Edges : good reflection Canopy: good reflection	GOOD
SUMMER	Body : no contrast (OK) Edges : good reflection Canopy: prominent ref Plume : good contrast	Same as JET GOOD	Body : visible Edges : prominent reflection Canopy: good reflection	GOOD
COOL	Body : not visible Edges : no reflection Canopy: good reflection Plume : only inner	BAD	Body : visible Edges : good reflection Canopy: good reflection	GOOD

9.6.3 Discussion on Results of Test Scenario No. 2

The results generated using the Test Scenario No 2 are analysed for the appearance of the IR signature representation in virtual reality. The results of test scenario No. 2 are discussed in the following paragraphs.

9.6.3.1 Different Colour-map

On the basis of the results shown in Table 9-8, it is suggested that the "*jet*" colour-map is the most suitable to represent the IR signatures in both the 3-5 and 8-12 bands. Also this colour-map shows the leading-edge reflections and canopy cold sky reflections. The "*summer*" colour-map may also be used to represent the IR signature in the 3-5 and 8-12 micron wavebands. The "*cool*" colour-map may represent the 8-12 micron waveband but this is not very clear in the 3-5 micron waveband. The "*hot*" colour-map may represent reasonably in the 3-5 micron waveband but this is not

realistic in the 8-12 micron waveband. The "*gray*", "*bone*" and "*HSV*" could not show the reflection effects.

9.6.3.2 Physical Properties vs Material Properties of VRML

The emissivity, reflectivity and transmissivity of the objects in the IR waveband may be related to the material properties of the objects in the virtual reality. The emissivity and temperature represent Radiance which may be shown by "*emissiveColor*" in VRML. The reflectivity is modelled by the "*DiffuseColor*" and the "*specularColor*" along with the "*ambientIntensity*" field of the material properties. The transmissivity is represented by the "*transparency*" field of VRML. Table 9-5 summarizes the suggestions for representing the IR signature of the different types of material in the virtual world. The different possibilities of material properties in VRML are tried and finally on the basis of visual appearance a strategy is suggested to represent the IR signature of a scene in the virtual reality. The summary of this option is given as under:

(a) **Dull Metallic Body.** The dull metallic body or surface may be shown as "*emissiveColor*" in VRML.

(b) **Gaseous Plume.** The exhaust gas plume of the aircraft may be shown as "*emissiveColor*" with "*transparency*" representing the transmissive nature of the gaseous plume.

(c) **Shining Leading-edges.** The leading-edges of the fast moving aircraft may be modelled as "*emissiveColor*", "*diffuseColor*" with "*ambienrtIntensity*" and "*specularColor*" with "*shininess*".

(d) **Cold Sky Reflections.** The cold sky reflection effects from the glass canopy depend upon the emissivity and reflectivity of the glass. The radiance of the canopy may be shown as "*emissiveColor*" and the sky radiance may be shown as the "*specularColor*" to represent the reflections of the sky from glass canopy.

9.6.3.3 Plume Radiance

From Figure 9-12 and Figure 9-15, the exhaust gas plume of the aircraft is the dominant source of radiation in the 3 to 5 micron wave band. Whereas, in 8 to 12 micron waveband the signatures of the plume are negligible as the spectral emissivity

of the plume is considered zero in the 8-12 micron waveband. In the 3-5 micron waveband the plume is the dominant source of radiation in the beam and the tail aspects as shown in Figure 9-12(a) and Figure 9-14(a) respectively. However, from nose aspect as shown in Figure 9-13(a) the plume is not visible.

9.6.3.4 Cold Sky Reflection from Glass Canopy

In the case of the glass canopy, out of the three physical properties, the transmissivity is neglected and only the effects due to emissive and reflective component are considered. The emissive component may cover the radiance of the canopy material and showing it as "*emissiveColor*". The reflective part may be covered by using "*specularColor*" corresponding to the radiance of the sky with "*shininess*" as reflectivity. But there is no "*diffuseColor*" on the canopy. To make sky reflections prominent an additional light source may be modelled to represent the sky or sun irradiance. Figure 9-18 to Figure 9-21 shows the IR signature of a target aircraft with and without cold sky reflection effects in the two IR wavebands of the 3-5 and the 8-12 micron. The effects of the cold-sky reflections from the canopy are prominent in the 3-5 and 8-12 micron wavebands in Figure 9-18(a) to Figure 9-21(a). The dark black canopy in Figure 9-18(b) and Figure 9-20(b) shows that the glass canopy has less emissivity and a significant effect is due to the reflection.

9.7 Explanation of the Test Scenario No. 3

In the test scenario No. 3 the sequence of events of an engagement of a passive IR imaging seeker homing missile with a flying target aircraft are simulated to analyse the missile lateral acceleration limit (LATAX), the tracking algorithms and the missile hit criterion. The scenario is planned as the air-to-air / surface-to-air missile is chasing an aircraft flying at 1000 meters altitude. The different manoeuvres of the aircraft are considered in straight and level and also in level turn. The missile is modelled for two different LATAX limits. The output results are presented in 2D and 3D plots and also as animated movie clips. The two tracking techniques (binary and intensity centroid tracker) are analysed for target location estimation. The missile hit criterion is analysed for impact from different aspects.

9.7.1 Inputs Data for Test Scenario No. 3

The input parameters for the missile and target aircraft required for test scenario No. 3 are explained in the following paragraphs.

9.7.1.1 Mode of Operation

The "air-to-air" and "surface-to-air" modes are used for the missile target engagement simulation.

9.7.1.2 Missile Parameters

Type of Missile	:	"air-to-air" and "surface-to-air"
Missile speed	:	Mach # 3 and Mach # 4
Missile load factor	:	20 G's and 40 G's
Seeker refresh rate	:	100 Hz
Hit criterion	:	5 meters
Initial position [X,Y,Z]	:	[0, 1000, 0] and [0, 0, 0]
Detector size	:	0.1 mm
Seeker Field-of-view	:	2^o
Pixel Image Size	:	256 x 256 pixels
Spectral Band coverage	:	3-5 and 8-12 μm

9.7.1.3 Atmospheric Parameters

The atmospheric parameters are selected on the basis of the "*good*" weather conditions as defined in Chapter-6 Table 6-4.

9.7.1.4 Background Input Parameters

Background upper Hemisphere	:	Three Layers of Sky
Type of Sky	:	Clear
Altitude of layers	:	sea level, 1000 meters, 10 km
Background lower Hemisphere	:	Ground
Temperature	:	290 K
Emissivity	:	0.9

9.7.1.5 Target Input Parameters

The target sub-parts, temperatures and radiometric properties are the same as listed in Table 9-4 for the test scenario No. 2. The other input parameters are given as follows:

Target aircraft speed	:	Mach # 2
Target aircraft load factor	:	9 G's
Target rate-of-descent	:	0 meters/sec
Target initial position	:	[2000, 1000, -4000],[2000, 1000, -2000]
Target manoeuvres	:	Straight and level left-to-right,
	:	Level-turn right away

9.7.2 Results of Test Scenario No. 3

The missile lateral acceleration limit is analysed by simulating the missile target engagement scenario with different missile speed and load factor values. The missile tracking algorithm is analysed for binary and intensity centroid tracker and the missile hit criterion is tested for approaching the target from different aspects. The results of test scenario No. 3 are produced in the following paragraphs.

9.7.2.1 Straight and Level Target in Air-to-air Mode

In this scenario the target aircraft is flying at an altitude of 1000 meters in the straight and level with a speed of Mach# 2. The target aircraft is crossing from left to right. The initial position of the aircraft in the world coordinates is [2000, 1000, -4000]. Figure 9-22 shows the missile chasing the target aircraft with two different LATAX conditions. In Figure 9-22(a) the missile has a constant speed of Mach# 3 and a load factor of 20 G's. Figure 9-22(b) shows the second condition of LATAX with the missile speed of Mach# 3 and load factor of 40 G's. In both cases the missile hits the target and the distance calculated from the centre of the target to the centre of the missile is 7.58 meters.

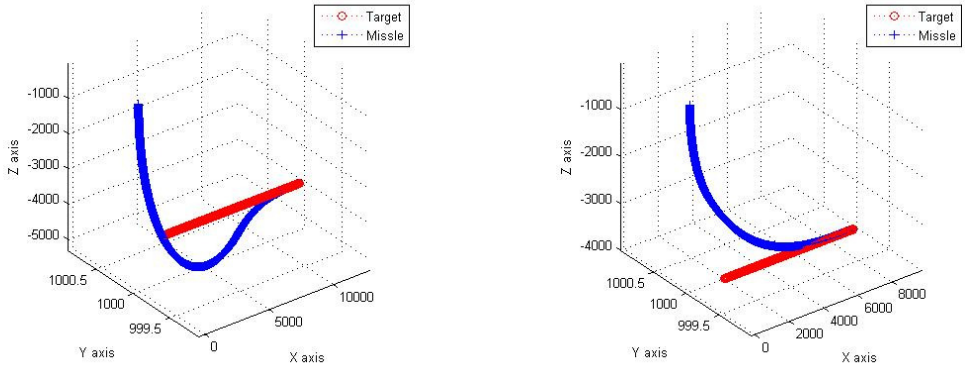

(a) Missile Mach# 3 and 20 G's (b) Missile Mach# 3 and 40 G's

Figure 9-22 : Air-to-air Missile chasing straight and level target aircraft

The 3D plots of Figure 9-22 are shown again in Figure 9-23 in 2D view to demonstrate the effects of LATAX on the missile-target engagement.

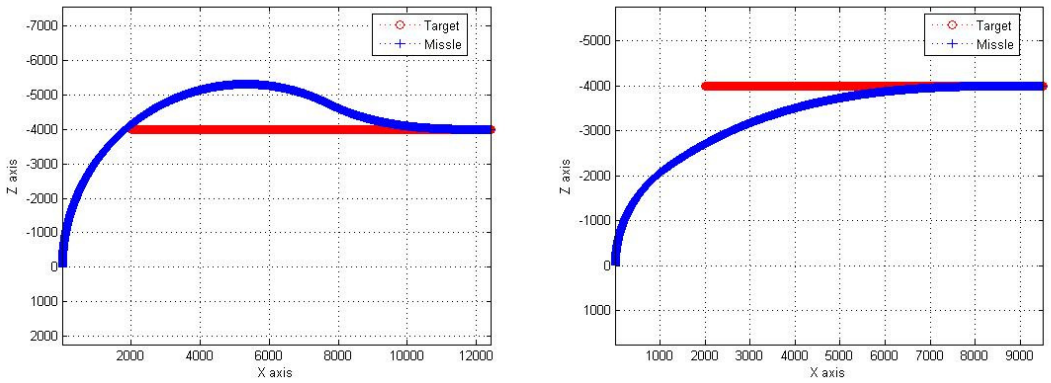

(a) Missile Mach# 3 and 20 G's (b) Missile Mach# 3 and 40 G's

Figure 9-23 : XZ-view of missile chasing straight and level target

9.7.2.2 Target Aircraft in Level-turn Chased by Air-to-air Missile

Figure 9-24 shows the flight path of the target aircraft and the missile in 3D world coordinates. The target aircraft is flying at a constant speed of Mach# 2 in level turn. The initial location of the target aircraft is [2000, 1000, -2000]. The missile is also flying at same altitude of 1000 meters. The initial location of the missile in world coordinates is at [0, 1000, 0]. The two sets of missile LATAX limits are modelled. Figure 9-24(a) and Figure 9-25(a) shows the missile with speed of Mach# 4 and a load factor of 20 G's. The second set of LATAX setting is for a speed of Mach# 3 and a load factor of 40 G's is shown in Figure 9-24(b) and Figure 9-25(b). With the LATAX setting of Mach # 4 and 20 G's, the missile misses the target. Whereas, for the LATAX setting of Mach# 3 and 40 G's, the missile hits the target with a miss-distance of 5.36 meters.

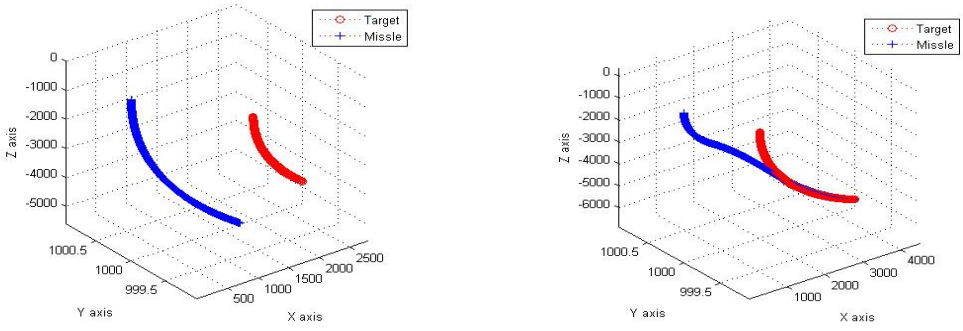

(a) Missile Mach# 4 and 20 G's (b) Missile Mach# 3 and 40 G's

Figure 9-24 : Air-to-air missile chasing the target aircraft in level turn

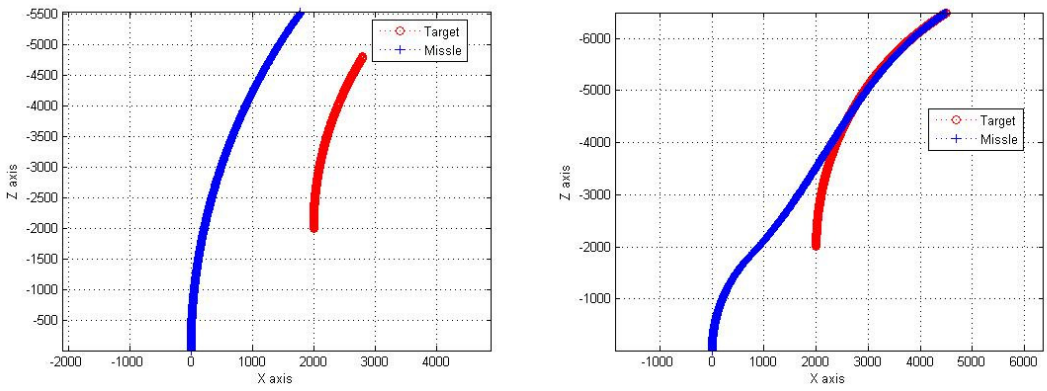

(a) Missile Mach# 4 and 20 G's (b) Missile Mach# 3 and 40 G's

Figure 9-25 : XZ-view of air-to-air missile chasing the target aircraft in level turn

9.7.2.3 Target Aircraft in Level-turn Chased by a Surface-to-air Missile

The third case is taken of an aircraft flying at an altitude of 1000 meters in a level-turn with a speed of Mach# 2 and a load factor or 9 G's. The initial position of the aircraft in world coordinates is at [2000, 1000, -2000]. The missile initial position is at ground level with world coordinates of [0, 0, 0]. Figure 9-26 shows the target and missile tracks for the two LATAX conditions. Figure 9-26(a) shows the LATAX setting for the speed of Mach# 4 and a load factor of 20 G's and Figure 9-26(b) shows the LATAX setting for a speed of Mach# 3 and a load factor or 40 G's. For the first LATAX setting the missile misses the target. Whereas, for the second setting the missile hits the target aircraft with a miss-distance of 6.10 meters.

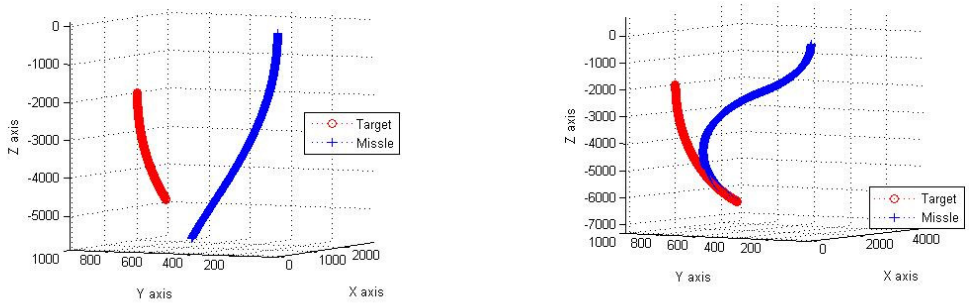

(a) Missile Mach# 4 and 20 G's (b) Missile Mach# 3 and 40 G's

Figure 9-26 : Surface-to-air Missile chasing a target in level-turn

The 3D plot of Figure 9-26 is shown in 2D views as XZ, YZ and XY in Figure 9-27, Figure 9-28 and Figure 9-29 respectively.

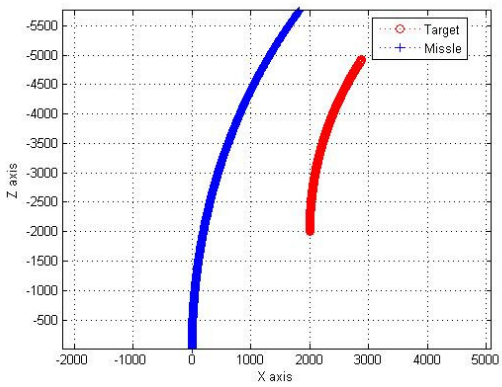

(a) Missile Mach# 4 and 20 G's

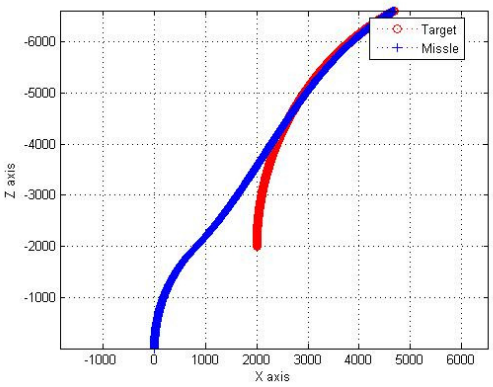

(b) Missile Mach# 3 and 40 G's

Figure 9-27 : XZ-view of surface-to-air missile chasing target in level-turn

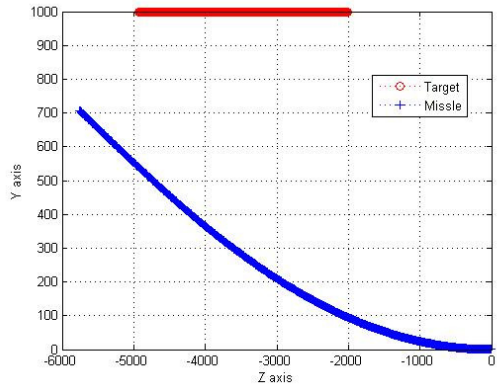

(a) Missile Mach# 4 and 20 G's

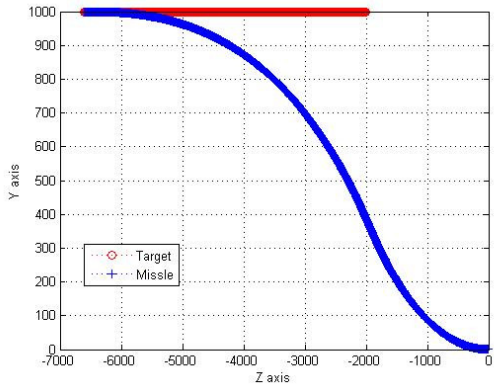

(b) Missile Mach# 3 and 40 G's

Figure 9-28 : YZ-view of surface-to-air missile chasing target in level-turn

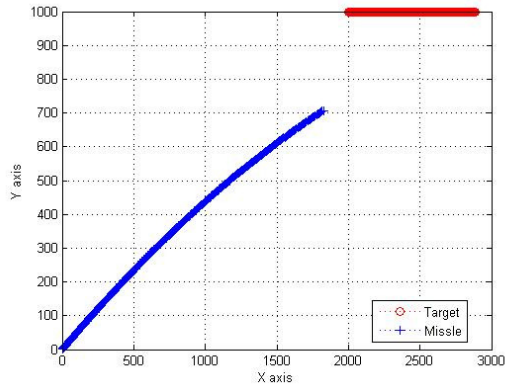

(a) Missile Mach# 4 and 20 G's

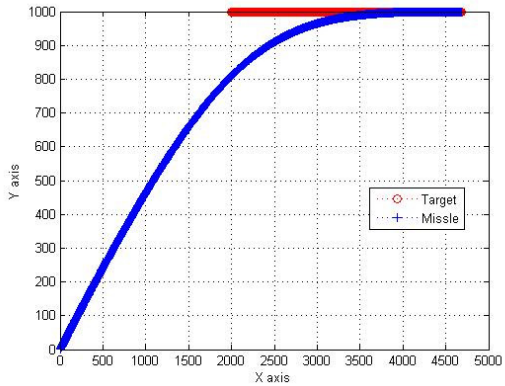

(b) Missile Mach# 3 and 40 G's

Figure 9-29 : XY-view of the surface-to-air missile chasing target in level-turn

9.7.2.4 Finding the Centroid using Binary and Intensity Centroid Trackers

The binary and intensity centroid tracker are modelled for target location estimation. Figure 9-30(a) shows the output of the binary centroid tracker with the centroid location denoted as the square at the coordinates of [121.02, 128.05]. The centroid found by the intensity centroid tracker is shown in Figure 9-30(b) as the square at [130.65, 128.01]. Figure 9-31(a) shows the output of the binary centroid tracker when a flare is present in the FOV. The small square denotes the coordinates of the centroid at [152.14, 136.17]. Similarly, with a flare within the FOV the centroid found by the intensity centroid tracker is shown in Figure 9-31(b) at [165.21, 139.47].

(a) Binary centroid tracker centroid [121.02, 128.05]

(b) Intensity centroid tracker centroid [130.65, 128.01]

Figure 9-30 : Centroid output of Binary and Intensity centroid trackers

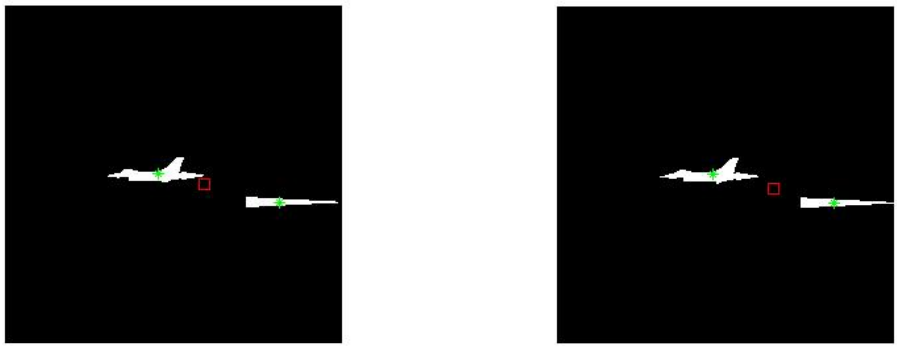

(a) Binary centroid tracker centroid [152.14, 136.17]

(b) Intensity centroid tracker centroid [165.21, 139.47]

Figure 9-31 : Centroid output of Binary and Intensity centroid trackers with flare

9.7.3 Discussion on Results of Test Scenario No. 3

The results of the test scenario No. 3 are used to analyse the effects of missile lateral acceleration on the missile-target engagement, the effects of binary and intensity centroid tracker on the target location estimation and the hit-criterion. The results of the test scenario No. 3 are discussed in the following paragraphs.

9.7.3.1 Missile Lateral Acceleration

The missile lateral acceleration affects the missile's ability to chase the target aircraft. The LATAX is analysed for three different cases; one with an air-to-air missile chasing an aircraft flying in straight and level path as shown in Figure 9-22 and Figure 9-23. The second case is of an air-to-air missile chasing an aircraft in a level-turn as shown in Figure 9-24 and Figure 9-25. The third case is of a surface-to-air missile chasing an aircraft in level-turn as shown in Figure 9-26 to Figure 9-29. In the first case shown in Figure 9-23, the two LATAX settings (of speed Mach# 3 and load factor of 20 G's and speed Mach# 3 and load factor 40 G's) are analysed. The missile hit the target aircraft with both LATAX settings. However, with a higher load factor as shown in Figure 9-23(b) the missile chased the target with a sharper manoeuvre as compared to Figure 9-23(a) with a long curved path. In the second and third cases, the two LATAX settings are selected as one with speed Mach# 3 and load factor 40 G's and other with speed Mach# 4 and load factor 20 G's. With the first LATAX setting the missile hit the target successfully as shown in Figure 9-25, Figure 9-27, Figure 9-28 and Figure 9-29. Whereas, with the second LATAX setting the missile is unable to steer to the target aircraft. Thus the missile control algorithm is taking care of the missile LATAX limits and it is shown that reducing the missile speed and increasing the load factor makes the missile manoeuvres more sharply.

9.7.3.2 Binary and Intensity Centroid Tracker

In the target location estimator algorithm, the two types of trackers are modelled, the binary centroid and the intensity centroid tracker. In Figure 9-30, the centroid found by the binary and intensity centroid trackers are shown as a square at location [121.02, 128.05] and [130.65, 128.01] respectively. Although, the difference in the two centroid values is not very significant, however, as compare to the binary centroid, the intensity centroid is slightly shifted towards the tail of the aircraft. This is because for the binary centroid the mass of each pixel is considered as unity irrespective of the

intensity of each pixel. Whereas, for the intensity centroid the mass of each pixel is as per the intensity or the normalized radiance of each pixel. Table 9-6 shows the normalized radiance values of different sub-targets for the 3-5 micron waveband. The normalized radiance of the exhaust gas plume is much more than the rest of the parts of the aircraft. Therefore, the intensity centroid is shifted towards the tail of the aircraft. Similarly, Figure 9-31 shows the output images with a flare present within the FOV. Due to the presence of the flare the centroid has moved towards the flare plume. In Figure 9-31 the centroid found by the binary centroid tracker is shown as a square at location [152.14, 136.17] and the centroid with the intensity centroid tracker is shown at location [165.21, 139.47]. In the case of the intensity centroid the centroid has shifted further towards the flare plume. This is because of the fact that the intensity of the flare plume is higher as compared to the different parts of the target.

9.7.3.3 Hit Criterion

The hit criterion given in Equation 8-88 of Chapter-8 is analysed for the missile hitting the target aircraft from different aspects. For the three cases of test scenario No. 3, the missile is considered to hit the target aircraft if the direct distance between the target and the missile (R_{TMD}) is less than the missile step ($step_{msl}$) and the length of the error vector (R_{err}) is less than the R_{impact} given as the input parameter. The R_{impact} is considered as two meters (which is about half the minimum length of the typical fighter aircraft). In first case of Figure 9-22, the missile hit the target as R_{TMD} is 7.58 meters which is less than the $step_{msl}$ (10.21 meters) and R_{err} is 0.02 meters which is less than R_{impact} (2 meters). Similarly, in the second case of Figure 9-24(b) the R_{TMD} is 5.36 meters and R_{err} is 0.018 meters which also meets the hit criterion. The third case of Figure 9-26(b) has R_{TMD} of 6.10 meters and R_{err} of 0.02 meters which also satisfies the hit criterion. The algorithm is therefore working fine with the hit criterion based on the cylindrical space in front of the missile. However, to increase the fidelity of the model a better logic for the hit criterion is required. This could be by replacing the missile step with some fixed distance (like half the length of the target) or even further improved by incorporating the "*collision*" and "*navInfo*" nodes of the VRML in the algorithm which may even consider the contour of the target for the hit criterion. This could be considered in future work.

9.8 Explanation of the Test Scenario No. 4

In the fourth test scenario the same target aircraft considered in test scenario No. 2 is now dispensing an expendable flare. The appearance of the target aircraft and the flare in the IR wavebands of 3-5 and 8-12 micron are analysed. The flare appearance in the virtual world is analysed in the static 2D mode. The radiance values of the flare are converted into a corresponding RGB colour-map. The IR signature of an aircraft and a flare at 1000 meters altitude is analysed from the seeker of an air-to-air missile at the same altitude. The distance between the target aircraft and the missile is kept as 1500 meters. The IR spectral bands of 3-5 and 8-12 micron are considered. The missile seeker is viewing the flare from the beam aspect.

9.8.1 Input Data for Test Scenario No. 4

The following paragraphs explain the inputs for the Test Scenario No. 4.

9.8.1.1 Mode of Operation

The mode of operation is kept as "air-to-air" for the LOWTRAN data runs.

9.8.1.2 Missile Parameters

Type of Missile	:	Air-to-air
Image Size in pixels	:	256 x 256 pixels
Spectral Band Coverage	:	3-5 and 8-12 μm
Range between target and missile	:	1500 meters
Seeker refresh rate	:	100 Hz
Initial position [X,Y,Z]	:	[0, 1000, 0]
Seeker Field-of-view	:	2^o

9.8.1.3 Atmospheric Parameters

The atmospheric parameters are selected on the basis of the "*good*" weather conditions as defined in Chapter-6 Table 6-4.

9.8.1.4 Background Parameters

Background upper Hemisphere	:	Three Layers of Sky
Type of Sky	:	Clear
Altitude of layers	:	sea level , 1000 meters, 10 km

Background lower Hemisphere	:	Ground
Temperature	:	290 K
Emissivity	:	0.9

9.8.1.5 Target Input Parameters

The target temperature, area and radiometric properties are the same as considered in test scenario No. 2 and are shown in Table 9-4.

9.8.1.6 Flare Input Parameters

The input parameters of the flare required for the test scenario No. 4 are as under:

Mass of the flare (m_{flare})	:	300 gm
Flare ejection velocity (V_{eject})	:	30 meters/sec
Flare eject angle (θ_{flare})	:	0^o to -90^o @ -15^o
Aircraft Speed ($V_{aircraft}$)	:	Mach # 0.68
Aircraft Location	:	[0, 1000, -1500]
Flare drag coefficient (C_D)	:	2.4, 1.5, 1.0, 0.5, 0.1
Atmospheric density (ρ_{air})	:	1.225 kg/m^3
Flare ejection time (t_{eject})	:	0.01 sec
Flare pallet dimensions	:	206x50x25 mm
Flare rise time (t_{rise})	:	0.2 sec
Flare burn time (t_{burn})	:	3.5 sec
Flare rise time constant (τ_{rise})	:	0.1
Flare burn time constant (τ_{burn})	:	6.0
Flare temperature inner layer	:	2000 K
Flare temperature outer layer	:	1000 K
Flare emissivity	:	0.95

The material field values for the two layers of the flare plume are given in Table 9-9.

Table 9-9 : Input material properties of the flare for test scenario No. 4

Sub-Target	Ambient Intensity	Diffuse Color	Emissive Color	Shininess	Specular Color	Transparency
Inner layer	0	0	$N_{flareinn}^*$	0	0	0
Outer layer	0	0	$N_{flareout}^*$	0	0	0.5

NOTE: The emissive colour of flare is calculated in RGB colours which correspond to the normalized radiance of each layer of the flare.

9.8.2 Results of Test Scenario No. 4

The numerical values of the flare radiance and the corresponding RGB colours are given in Table 9-10 for the 3-5 micron waveband and the values for the 8-12 micron waveband are given in Table 9-11.

Table 9-10 : Outputs of test scenario No. 4 for 3 to 5 micron waveband

VARIABLE	UNITS	I	II
Flare Total Radiance (two layers)	W m^{-2} sr^{-1}	4.8382 $x10^{4}$	0.6180 $x10^{4}$
Flare Total Radiance after attenuation	W m^{-2} sr^{-1}	1.1716 $x10^{-13}$	0.1650 $x10^{-13}$
Maximum Radiance	W m^{-2} sr^{-1}	1.1716 $x10^{-13}$	
Normalizing Factor		2.1851 $x10^{+15}$	
Flare Normalized Radiance (two layers)		256	36.0751
Colour of Flare Plume (two layers)	Red Green Blue	0.5 0.0 0.0	0.0 0.625 1.0

Table 9-11 : Outputs of test scenario No. 4 for 8 to 12 micron waveband

VARIABLE	UNITS	I	II
Flare Total Radiance (two layers)	W m^{-2} sr^{-1}	4.7881 $x10^{3}$	1.5214 $x10^{3}$
Flare Total Radiance after attenuation	W m^{-2} sr^{-1}	0.5954 $x10^{-15}$	0.1957 $x10^{-15}$
Maximum Radiance	W m^{-2} sr^{-1}	0.5954 $x10^{-15}$	
Normalizing Factor		4.2999 $x10^{+17}$	
Flare Normalized Radiance (two layers)		256	84.1298
Colour of Flare Plume (two layers)	Red Green Blue	0.5 0.0 0.0	0.0 0.8125 1.0

9.8.2.1 Flare Spectral Response

Figure 9-32 shows the output images of the target aircraft and the flare in the 3-5 and 8-12 micron waveband from the beam aspect at a range of 1.5 km. The same images of the target aircraft and the flare are shown in Figure 9-33 without the background.

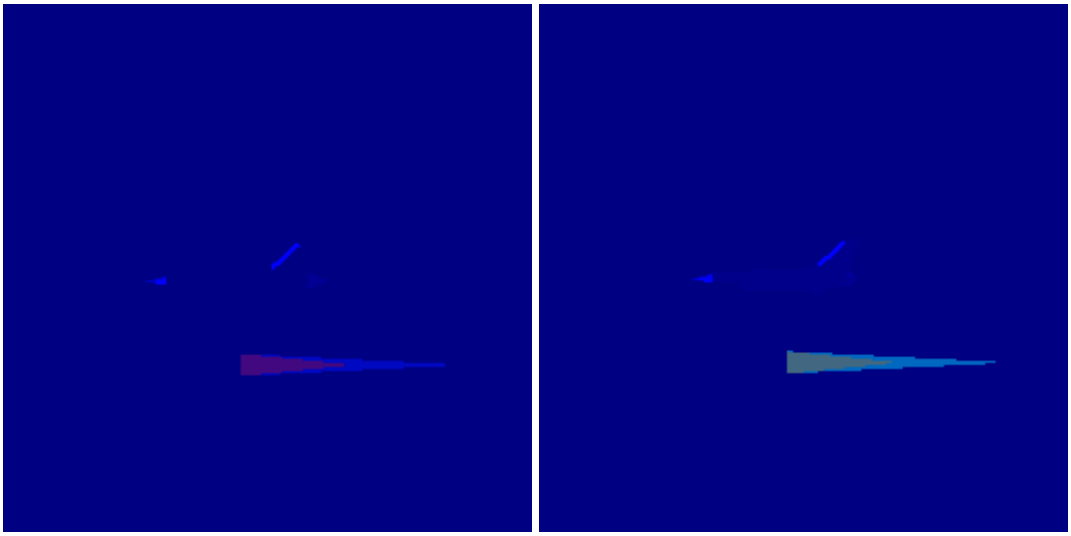

(a) 3 to 5 micron (b) 8 to 12 micron

Figure 9-32 : 256x256 image of aircraft with flare at 1.5 km range from beam aspect

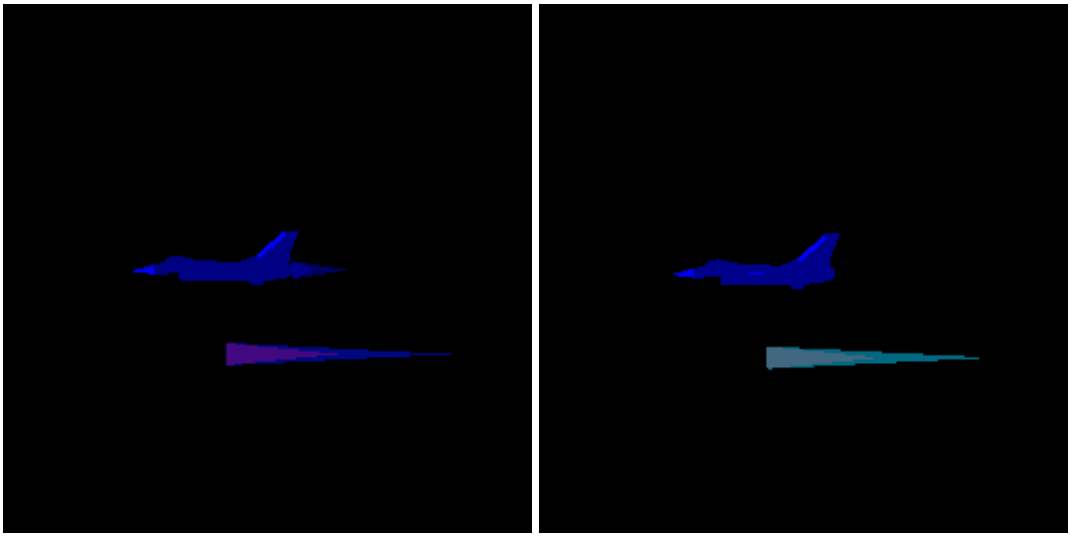

(a) 3 to 5 micron (b) 8 to 12 micron

Figure 9-33 : 256x256 image of aircraft with flare at 1.5 km range without background

9.8.2.2 Flare Temporal Response

Figure 9-34 shows the temporal response of the flare. The flare is dispensed after one second from the start of the simulation (t_{eject} = 1.0 sec). The temporal response is plotted for the input values of the rise time/burn time and rise/burn time constants as shown in Figure 9-34.

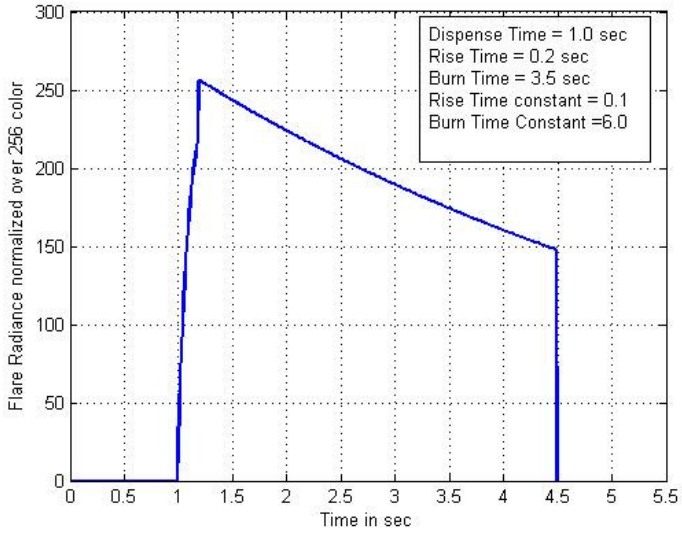

Figure 9-34 : Flare temporal response

9.8.2.3 Affect of Physical Parameters on Flare Trajectory

The flare trajectory is dependent upon several physical parameters of the flare pallet. The affects of the coefficient of drag (C_D), the mass of the pallet and the eject angle on the flare trajectory are analysed. To monitor the effect of the C_D, all other parameters are kept constant. The flare trajectory for the duration of the total burn (t_{burn} = 3.5 sec) is plotted for different values of the C_D such as 2.4, 1.5 and 1.0. Figure 9-35 shows the trajectory of a 300 gm flare pallet for the three values of the C_D when the flare is ejected downward. The same is plotted again in Figure 9-36 for the flare ejected in a forward direction.

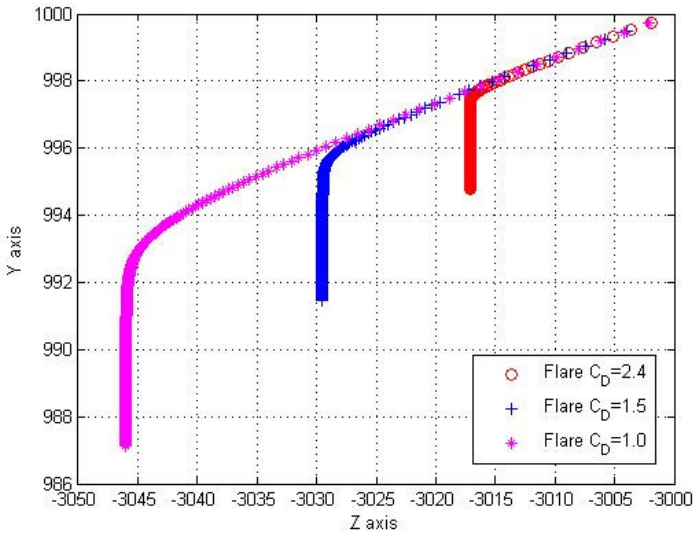

Figure 9-35 : Affect of C_D on 300 gm flare eject downward

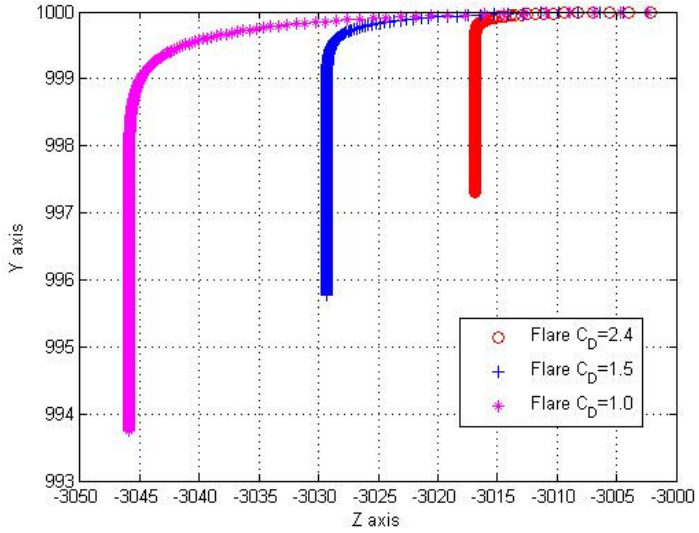

Figure 9-36 : Affect of C_D on 300 gm flare ejected forward

The affect of the mass of the pallet on the flare trajectory is analysed by keeping the other parameters constant and changing the mass. The trajectories for three values of the mass (100 gm, 300 gm and 1.0 kg) are plotted for two different ejection directions. Figure 9-37 shows the flare trajectories for a flare ejected downward and Figure 9-38 plots the same trajectories for the flare ejected in forward direction. The C_D is kept constant at 1.0 and the eject velocity is 30 meters per second.

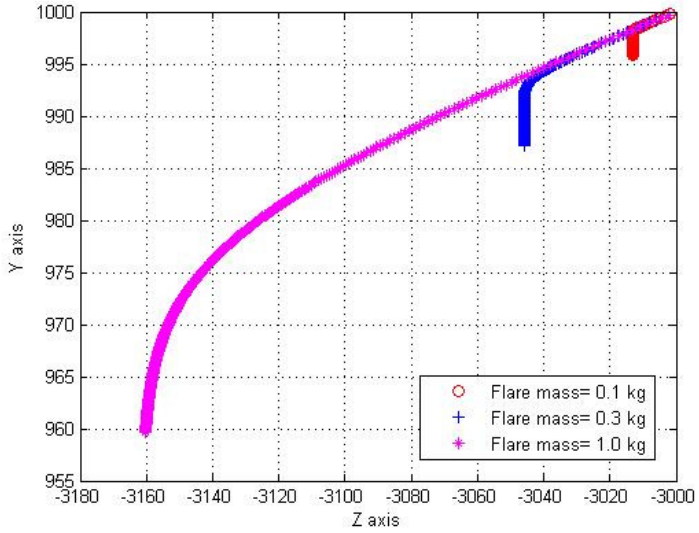

Figure 9-37 : Affect of pallet mass on trajectory for flare fired downward

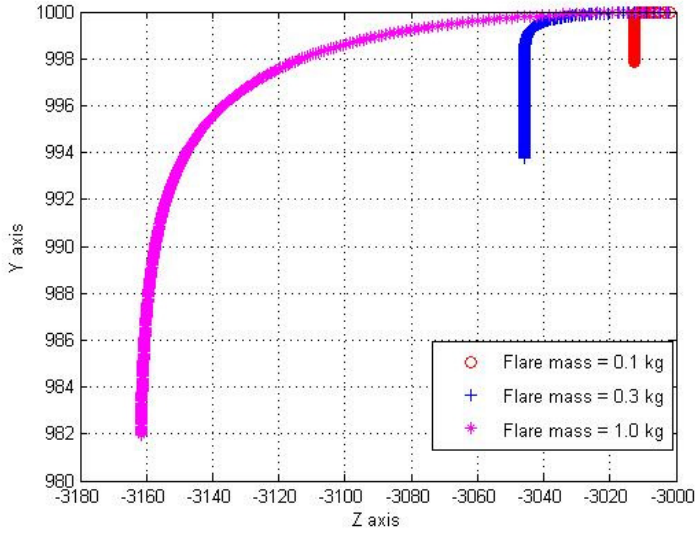

Figure 9-38 : Affect of pallet mass on trajectory for flare fired forward

The affect of the ejection angle on the flare trajectory is analysed for seven different values of eject angle between forward eject and downward eject. The negative pitch is increased in steps of 15 degrees. Figure 9-39 shows the plot of flare trajectories for the different eject angles. The other parameters are kept constant such as C_D is 1.0, mass of the pallet is kept as 300 gm and the eject velocity is 30 meters per second.

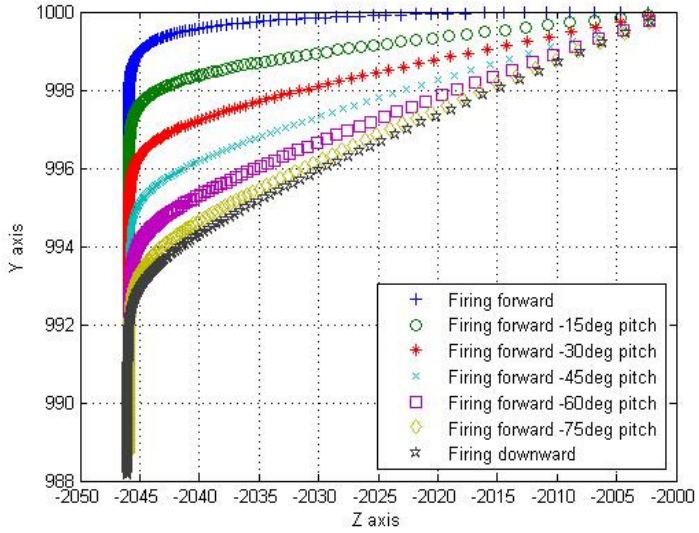

Figure 9-39 : Flare trajectory for different eject angles

9.8.3 Discussion on Results of Test Scenario No. 4

The results of the test scenario No. 4 are analysed for the flare spectral and temporal responses and the affects of the flare physical parameters on the trajectory which the flare makes after leaving the host aircraft. The results of test scenario No. 4 are discussed in following paragraphs.

9.8.3.1 Spectral and Temporal Responses of the Flare

The different numerical values of the flare for the 3-5 and 8-12 micron waveband are given in Table 9-10 and Table 9-11 respectively. The 256x256 image of the target aircraft and the flare are shown in Figure 9-32 and Figure 9-33. The flare is the most dominant source of radiation in both the 3-5 and 8-12 micron wavebands. Figure 9-34 shows the temporal response of the flare. During the rise-time (t_{rise} = 0.2 sec) the flare normalized radiance increases from a zero value to the peak value of 256. After the rise-time the flare radiance starts decreasing and reduces to the minimum value of 150 after the burn time (t_{burn} = 3.5 sec). The slope of the decaying curve is controlled by the burn time constant (τ_{burn} = 6.0) and may be altered to model the desired temporal response.

9.8.3.2 Affect of Coefficient of Drag (C_D) on Flare Trajectory

Figure 9-35 shows the trajectory of the flare ejected downward for the three different values of C_D. The higher the value of C_D the less distance the flare travels in the same time. With a C_D of 1.0 the flare travels about 46 meters in the horizontal direction and drops down to about 13 meters. Whereas, the flare of C_D 2.4 only travel 17 meters in the horizontal direction and 5 meters in the vertically downward direction. Hence, reducing C_D will make the flare travel a greater distance in both the horizontal and vertical directions. Figure 9-36 shows the same three conditions of C_D but with forward firing. For the same value of C_D, in both cases, the flare travels the same distance in the horizontal direction. However, for the same value of C_D with forward firing the flare travels a lesser distance in the vertically downward direction.

9.8.3.3 Affect of Mass of Pallet on Flare Trajectory

Figure 9-37 shows the flare trajectory for three different values of the pallet mass. The 0.1 kg flare pallet travels about 15 meters in the horizontal direction and about 5 meters in the vertically downward direction. By increasing the mass to 1.0 kg the flare

travels a much larger distance of 160 meters in the horizontal direction and about 40 meters downward. Hence increasing the mass of the flare makes it travel longer distances both in the vertical and horizontal directions. Comparing the 1.0 kg mass trajectory for the two different firing directions as shown in Figure 9-37 and Figure 9-38, the flare travels the same horizontal distance in both cases. However, with forward firing for the same mass the flare travels about half (about 18 meters) in the vertical direction as compared to the firing downward in which the same flare travels 40 meters.

9.8.3.4 Affect of Eject Angle on Flare Trajectory

Figure 9-39 shows the flare trajectory for different firing angles. The data is plotted for the firing angles from 0^o for firing forward to -90^o for firing downward with a step of -15^o. In all cases the horizontal distances which the flare travels is the same, whereas, the vertical distance reduces as the flare firing angle is reduced or is fired forward.

9.9 Validation of Results

In the case of visual imagery rendered for games, movies or other human consumption, the realism is based on a judgement of what "looks good" to the human eye. However, in the case of sensor rendering (e.g. missile sensor), the human eye responses are not necessarily relevant and can even be misleading. Instead, the most reasonable approach may be to have a relevant physics based approach [OLS03]. The validation is concerned with how well the model represents the actual physical process. Accuracy and realism are the two main attributes which need to be validated by comparing the results with some measured data. Accuracy relates to the correctness of the mathematical model to characterise some physical process, whereas, the realism means how close to reality the system is in appearance.

9.9.1 Need for Validation

Verification is the process of ensuring the simulation is a faithful representation of the intended underlying conceptual models [VAI99]. The decision makers need confidence that models and simulations are fit to support their decision making process, such that their decisions are useful to their specific project or program [MAG01]. The accuracy of the modelling and simulation process may be considered

crucial in mission critical applications such as missile-target engagement and IRCM analysis for maximizing platform survivability in combat.

9.9.2 Validation Methods

The first step in the validation process is to look at Figures-of-Merits (FOMs) that are representative of the scene. In the IR signature model the FOMs could be the radiance and the power received at the detector from the sub-targets and the backgrounds. Subsequently, in rendered scene the FOMs could be the corresponding colour of every pixel and the material properties such as the emissivity, reflectivity and transparency. The values of all the pixels over the entire field-of-view may be shown in the form of an image of the scene. The FOMs for the missile validation could be its lateral acceleration, tracking algorithm and hit-criterion. The FOMs for the flare validation could be the ballistic trajectory, spectral and temporal responses. The method for validating the simulation results could be to compare the response of both the real and simulated systems by using matched input test conditions and, therefore, to ensure that the output responses also match. Ideally, the IR signature model is to be validated by extensive comparison with measured data sets. However, the parameters of the military IR systems (heat-seeking missiles, IRCM and military aircraft IR signatures etc.) are often classified data and thus are not available for validation [CHR01]. As an alternate approach, comparing the results with some other computer based model which has been validated with measured data may be considered as a logical method for validation.

9.9.3 Flare Trajectory Validation

The deceleration of a flare can be represented by Equation 9-1 [POL93].

$$a_{flare} = \frac{dV}{dt} = \frac{\rho_{air} g v^2}{2\beta} \qquad \textbf{(9-1)}$$

where,

a_{flare} is the flare deceleration due to drag

ρ_{air} is atmospheric density

v is the velocity

β is the ballistic coefficient

g is the acceleration due to gravity

The ballistic coefficient β is defined as

$$\beta = W / C_D A_{ref} \qquad \textbf{(9-2)}$$

where,

W is the weight of the flare which will vary with time

C_D is the drag coefficient (different values for supersonic and subsonic)

A_{ref} is the reference area

David H. Pollock and Joseph S. Accetta in their book [POL93] have shown the flare separation relative to the dispensing aircraft for a variety of flight conditions. The flare trajectory plots as dispensed from an aircraft flying with different speeds at an altitude of 1500 meters are shown in Figure 9-40. These trajectory estimates are for the cylindrical flare with the following parameters:

(a)	Mass of flare	:	500 gm
(b)	Flare eject velocity	:	30 ms^{-1}
(c)	Flare eject angle	:	-90 deg (downward)
(d)	Flare burn time	:	4 sec

The data were generated by numerical integration of Equation 9-1 with continuous correction for the change in β as the flare burns. These values have shown agreement to within 10% of flight measurements [POL93]. The flare trajectory algorithm used in my work is validated against these plots shown in Figure 9-40. The flare separation relative to the dispensing aircraft for the same set of flight conditions as mentioned above are generated by running simulations. The simulated flare separation data for four airspeeds is plotted in Figure 9-41.

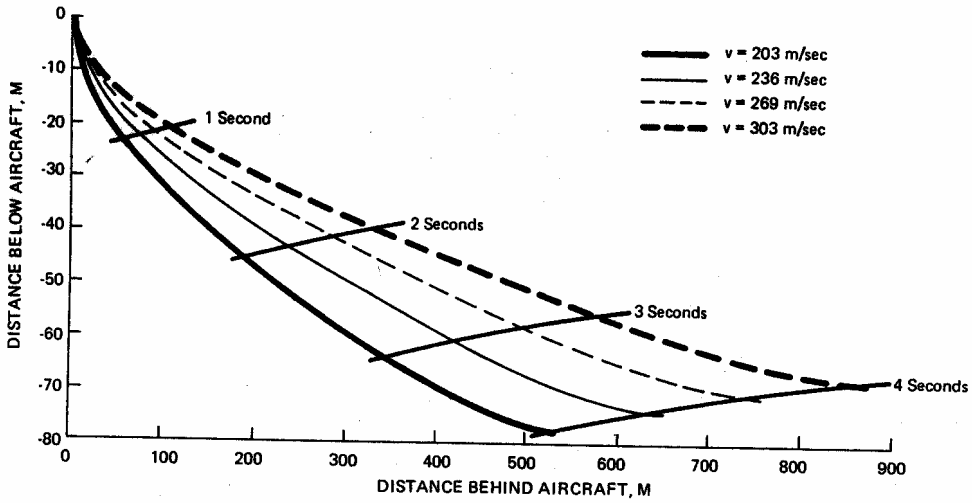

Figure 9-40 : Flare separation for selected airspeeds at 1500 meters altitude (source [POL93])

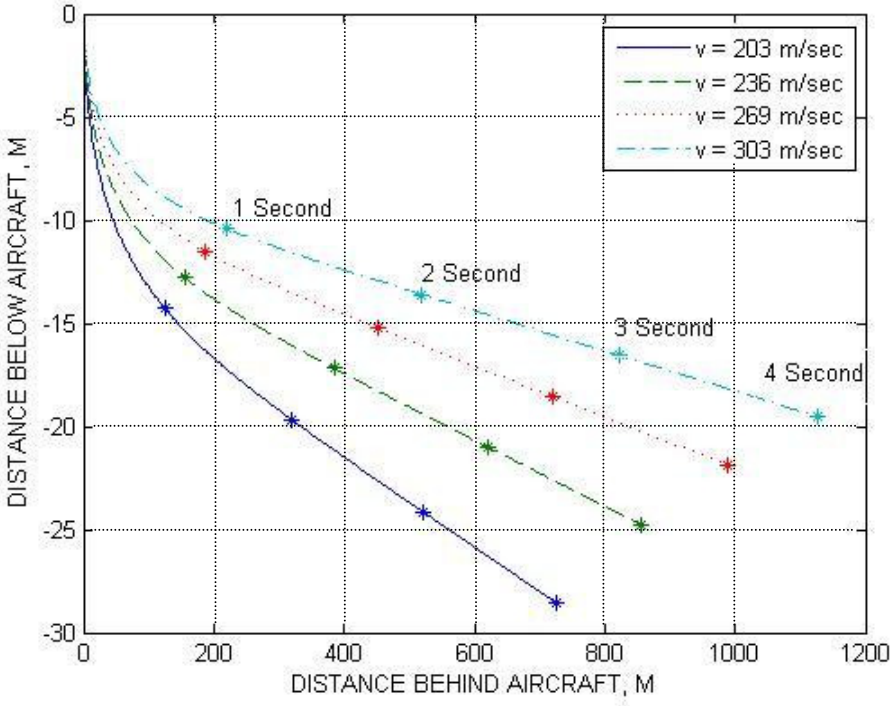

Figure 9-41 : Simulated flare separation for selected airspeeds at 1500 meters altitude

9.9.3.1 Discussion on Flare Trajectory Validation Results

The simulated data plotted in Figure 9-41 is showing the same trend as shown by the actual data plotted in Figure 9-40. However, in the simulated data for all four speeds, the maximum distance the flare has travelled behind the aircraft is greater (about 150 to 250 meters as speed is increasing) and the distance below the aircraft is less (about

50 meters) as compared to the actual data of Figure 9-40. This is because in the real world, as the flare burns, the flare trajectory takes account of the change in the ballistic coefficient β as given in Equation 9-2. Due to this the deceleration is very high near burnout and the flare drops more and slows down rapidly. Whereas, in the simulated data shown in Figure 9-41, the effects of the flare burnout on the ballistic coefficient are not considered. That means the flare pallet cross-sectional area, the drag coefficient and the mass are not varying as the flare burns. Therefore, the rate-of-separation is not very fast near burnout as is shown in the actual data of Figure 9-40. However, the variations in the ballistic coefficient due to flare burnout may be considered in future work by modelling linear change of mass with time and cross-sectional area with time.

9.9.4 Missile LATAX and Centroid Tracking Algorithm Validation

In the missile control and tracking algorithm, the capability of the missile to steer in 3D is limited by the implementation of the lateral acceleration limit of the missile. Depending upon the aspect of the engagement, the missile's ability to hit a target aircraft depends upon the lateral acceleration. In the Test Scenario No. 3 given in paragraph 9.7 above, the missile simulates two different lateral acceleration values. In the first case shown in Figure 9-26(a) to Figure 9-29(a) the missile LATAX is based on Mach# 4 and a load factor of 20 G's. Due to a higher turn-radius (*TR*) and lower rate-of-turn (ROT) the missile is unable to hit the aircraft. With a better LATAX value by reducing the speed to Mach# 3 and increasing the load factor to 40 G's, the missile has hit the target aircraft. This is shown in Figure 9-26(b) to Figure 9-29(b). Hence the missile guidance algorithm is taking care of the lateral acceleration of the missile.

The binary and intensity centroid tracker outputs are shown in Figure 9-31 (a) and (b) respectively. The binary and intensity centroid tracker algorithms have been validated by hand calculations performed on an example of a 10x10 pixel image shown in Figure 8-14 and Figure 8-15 respectively. The centroids are found by doing hand calculations using Equation 8-48 and 8-49 and are compared with the centroid found using the centroid tracker algorithms. The two results were matching perfectly. The hand calculations are not shown in the report but are available for verification.

9.9.5 Validations of Code

The Limited validation of the code has been done with the help of the available published results and comparing the rendered scenes visually with other reference outputs. Table 9-12 summarizes the validations performed during this work.

Table 9-12: List of validation of code

Feature	Validation method	Remarks
Total radiance of targets	Given same set of input temperature, emissivity and waveband, the numerical output of integral is compared with that of CounterSim calculations	Validated against CounterSim numerical results
Intensities of rendered IR scene	High and low values of normalized intensities observed against the expected RGB colour_index of selected colourmap	Numerically and visually validated
Targets radiometric properties in virtual reality	On aircraft, the shining leading-edge, dull metal skin, exhaust gas plume and reflections from glass canopy are visually compared with outputs of IR imaging systems and CounterSim simulator	Limited validation based on visual observations
Selecting "jet" colourmap	The images with same radiometric properties and in waveband are rendered with different colourmap. Based on the visual appearance of IR scene the "jet" colourmap is considered most suitable for representing IR intensities in RGB colours.	Validated based on visual observations
Missile lateral acceleration	Missile lateral acceleration is validated by varying speed and load factor one at a time and comparing the missile trajectory and the miss-distance during simulation	Numerically Validated
Centroid tracker algorithm	Binary and intensity centroid tracker algorithm is validated by taking an example of 10x10 pixels image and comparing results of code with hand calculations	Validated against hand calculations
Target trajectories	Planned manoeuvres observed visually on VR viewer and also monitoring the 3D plots of the target trajectories	Validated based on visual observations
Hit criterion	calculating distance between centre points of target and missile and comparing it with cylindrical volume in from of the missile to decide hit and calculating miss-distance	Numerically Validated
Flare trajectory	Validated against published measured data by comparing trajectories plotted for same input data sets	Validated against published data
Flare spectral response	Validated against given same set of input temperature, emissivity and waveband, the numerical output of integral is compared with that of CounterSim calculations	numerically Validated
Temporal response	The rise and fall curves plotted for different sets of time constants and observing the flare intensities on time scale	numerically Validated
Fast jet aircraft self protection level against kinematic CCM missile	Comparing results of simulations performed for same set of conditions and inputs on CounterSim IRCM simulator and analysing the self-protection level of two simulators	Limited validation against published simulator results
Atmospheric transmittance and sky radiance data sets	Calculated using LOWTRAN atmospheric transmittance code which is industry benchmark and has been validated against measured data sets	LOWTRAN validated against measured data sets

9.10 IRCM Analysis and Validation using Published Results

The aim of IRCM analysis is to see the affects of the different types of flare, firing angles, firing timings, missile-target aspects and aircraft manoeuvres on the missile miss-distance. This analysis could be used to determine the best characteristics of a decoy munitions and the optimum deployment position and timings. To validate the performance of the IR signature modelling and simulation, the IRCM analysis results are compared with published results [RIC06].

9.10.1 IRCM Analysis Scenario Generation and Input Parameters

The scenario of a heat-seeking missile firing at an aircraft dispensing flares and flying in a straight-and-level mode is simulated. Standard and aerodynamic expendable flares are dispensed with different firing angles to analyse the affect on the missile miss-distance. The input parameters used in the simulation [RIC06] using CounterSim are listed in Table 9-13 along with the input parameters used to simulate the same scenarios on my simulator. One target aircraft flying at constant speed of 450 knots (0.68 Mach#) is being chased by a surface-to-air missile with kinematic CCM (forward-bias) from different aspects between head-on to tail-chase with 30 degree steps. The aircraft altitude/range ratio is kept as 0.2286. The background is taken as clear sky. One flare is fired once the missile-target ranges are 1 km to 4 km in steps of 1 km. The hit criterion is taken as if the target comes within a radius of 5 meters of the missile. Any miss-distance between 5 to 10 meters is considered as near-miss and beyond 10 meters is a miss.

9.10.2 Comparison of Results of First IRCM Analysis Approach

The results of the fast jet analysis carried out in the reference [RIC06] are used to validate my work. The results given in the reference are for the following four flare settings. The polar plots of these results are shown in Figure 9-42 to Figure 9-45 respectively.

(a) Standard flare C_D 10.0, firing backward.

(b) Standard flare C_D 10.0, firing straight forward.

(c) Standard flare C_D 10.0, firing downward.

(d) Aerodynamic flare C_D 1.0 fired forward @ -30 deg pitch.

Table 9-13 : Input parameters for IRCM Analysis

	Input Parameters CounterSim	**Input Parameters My simulator**	**Remarks**
TARGET			
Speed	Mach# 0.68 (450 kts)	Mach# 0.68 (450 kts)	Same
Altitude/Range Ratio	0.2286 constant	0.2286 constant	Same
Data Points	1-4 km @ 500m and 0-180^O @ 30^O	1-4 km @ 1 km and 0-180^O @ 30^O	points at 1 km step only
Flight Mode	Straight and level	Straight and level	Same
MISSILE			
Speed	Mach# 2 (1323 kts)	Mach# 2 (1323 kts)	Same
Load factor	25 G's	40 G's	Increased
Seeker FOV	2 degree	2 degree	Same
Waveband	3-5 micron	3-5 micron	Same
Guidance	Proportional Navigation (max. lead angle of 17^o)	Pursuit-Course Guidance	PN guidance not implemented in my algorithm
Counter-countermeasure	Relative kinematic (forward bias)	Relative kinematic (forward bias)	CCM implemented at later stage
FLARE			
Rise time	0.2 sec	0.2 sec	Same
Burn time	3.5 sec	3.5 sec	Same
C_D for standard flare	10.0	10.0 and 2.4	Used two values
C_D for aerodynamic flare	1.0	1.0 and 0.1	Used two values
Firing angles	Backward, downward and forward firing with pitch 0^o to -90^o, @ -15^o	Backward, Downward, and forward firing with 0^o, -45^o and -90^o pitch	Only three angles used in forward firing

The polar plots of Figure 9-42 shows an aircraft in the centre and each crossing point around aircraft depict the missile launce position. The circles are at 1 km distance and show the missile-target range. The diagonal lines show the aspect from which the missile is approaching the target. Each line is at 30 deg steps between head-on and tail-on. The legend "decoy" shows the missile has miss the target and "no-decoy" means the IRCM flare was not effective and the missile has hit the target.

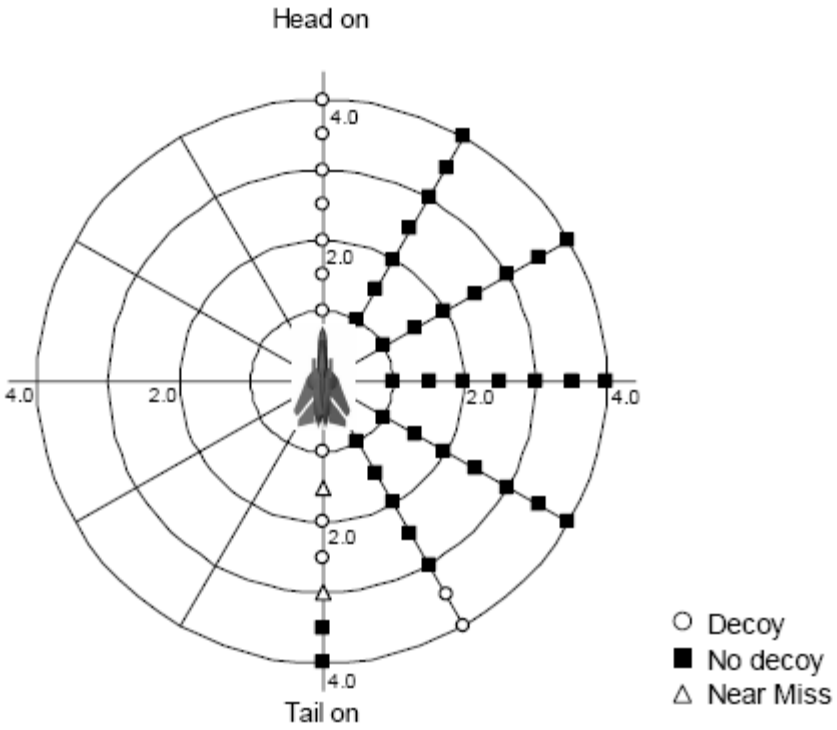

Figure 9-42 : Typical fast jet deploying standard flare fired backward (source [RIC06])

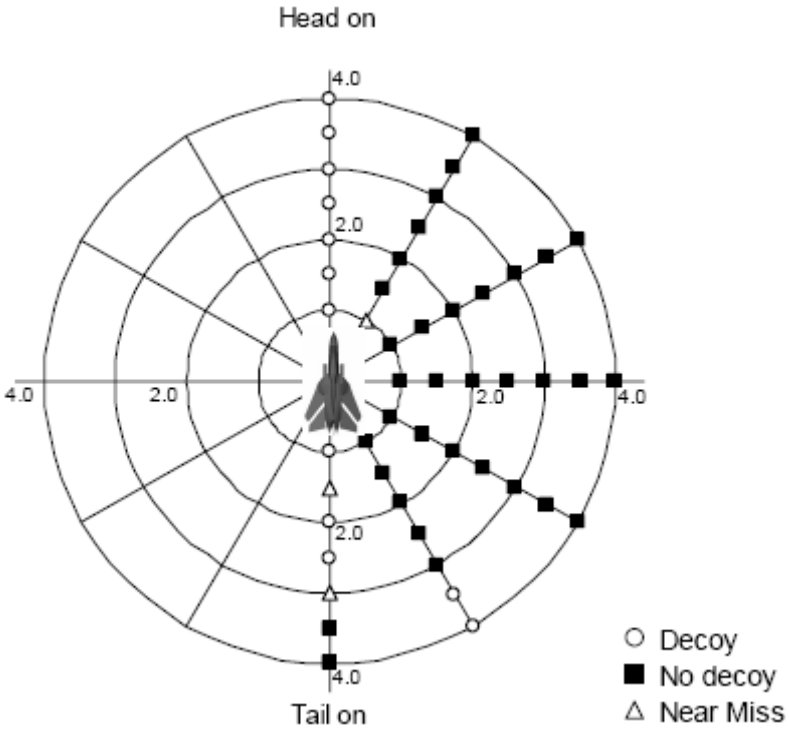

Figure 9-43 : Fast jet deploying standard flare fired straight forward (source [RIC06])

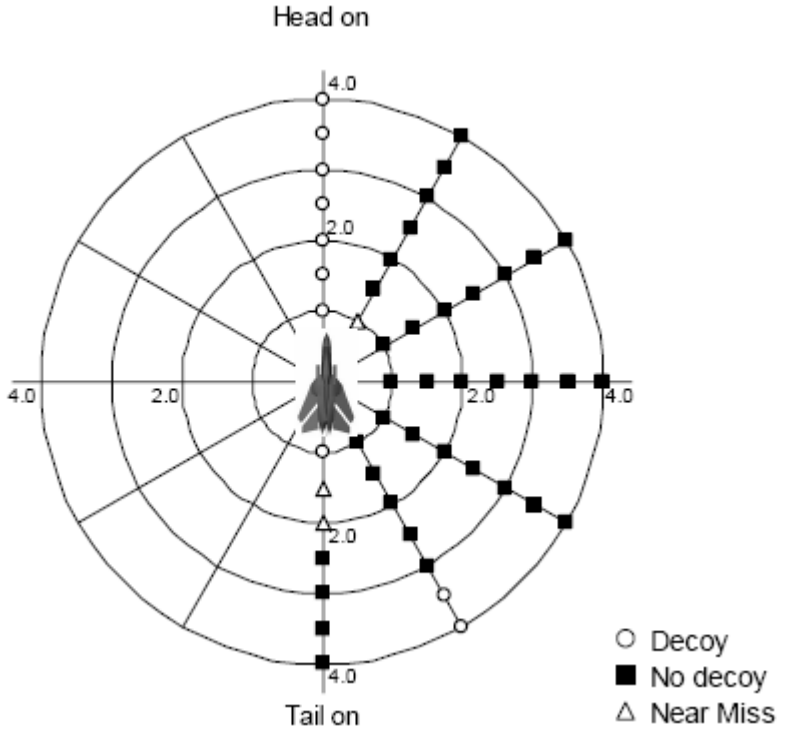

Figure 9-44 : Fast jet deploying standard flare fired downward (Source [RIC06])

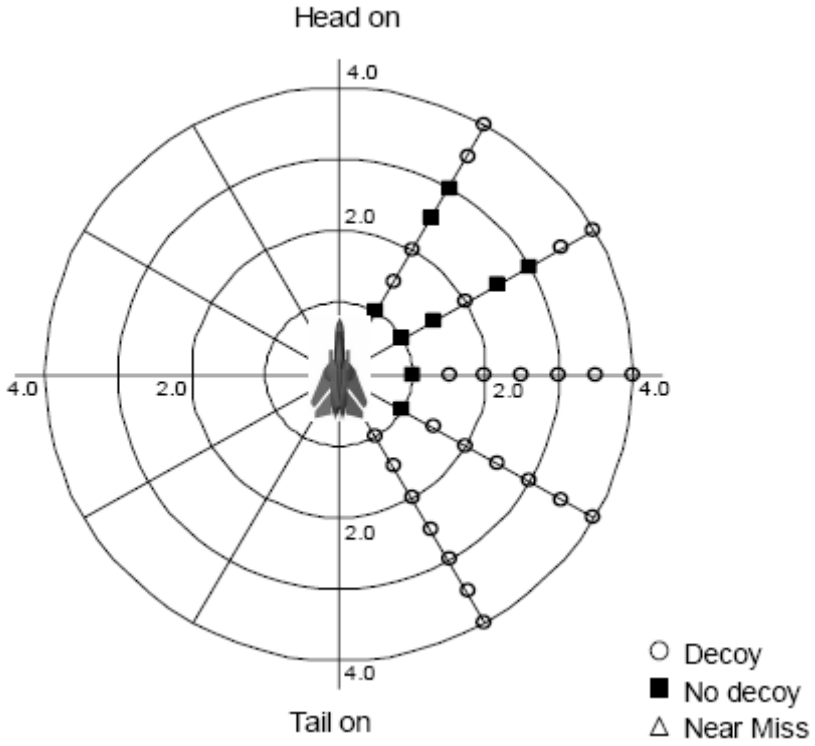

Figure 9-45 : Aerodynamic flare C_D 1.0 fired forward @ -30^o pitch (source [RIC06])

Using the input parameters shown in Table 9-13 the simulations are performed for the following setups. The results of following setups are compiled and are shown as the polar plots in Figure 9-46 to Figure 9-48 respectively and are summarized in Table 9-14.

(a) Standard flare C_D 2.4, firing downward, fired straight forward and fired forward with -45 deg pitch.

(b) Aerodynamic flares C_D 1.0 firing downward, fired straight forward and fired forward with -45 deg pitch.

(c) Aerodynamic flares C_D 0.1 firing downward, fired straight forward and fired forward with -45 deg pitch.

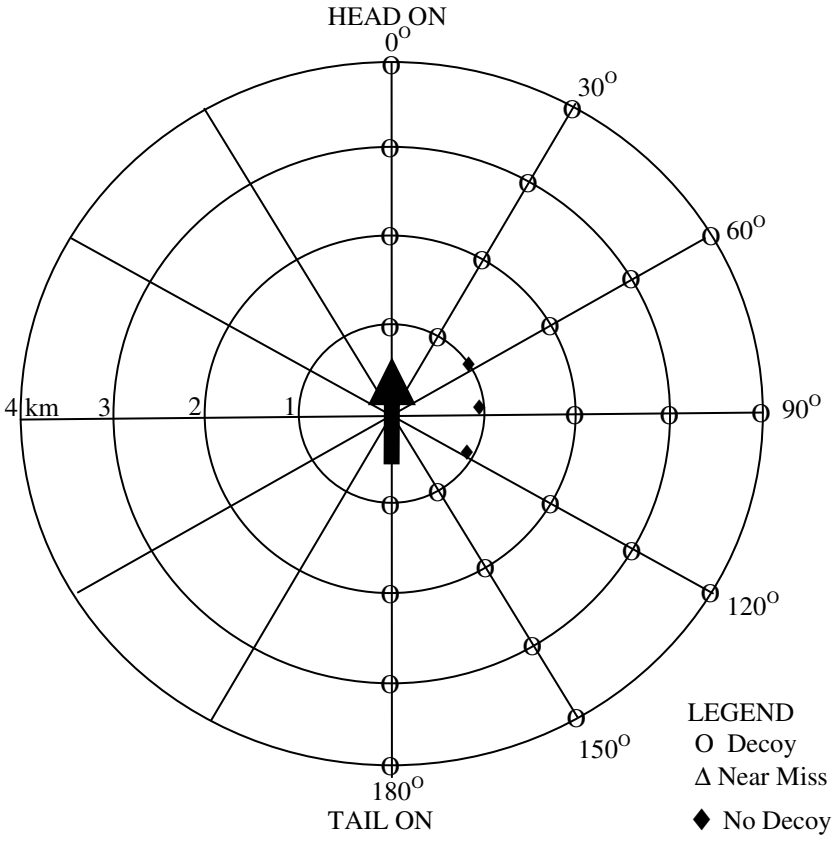

Figure 9-46 : Fast jet deploying standard flare C_D 2.4 fired in different directions

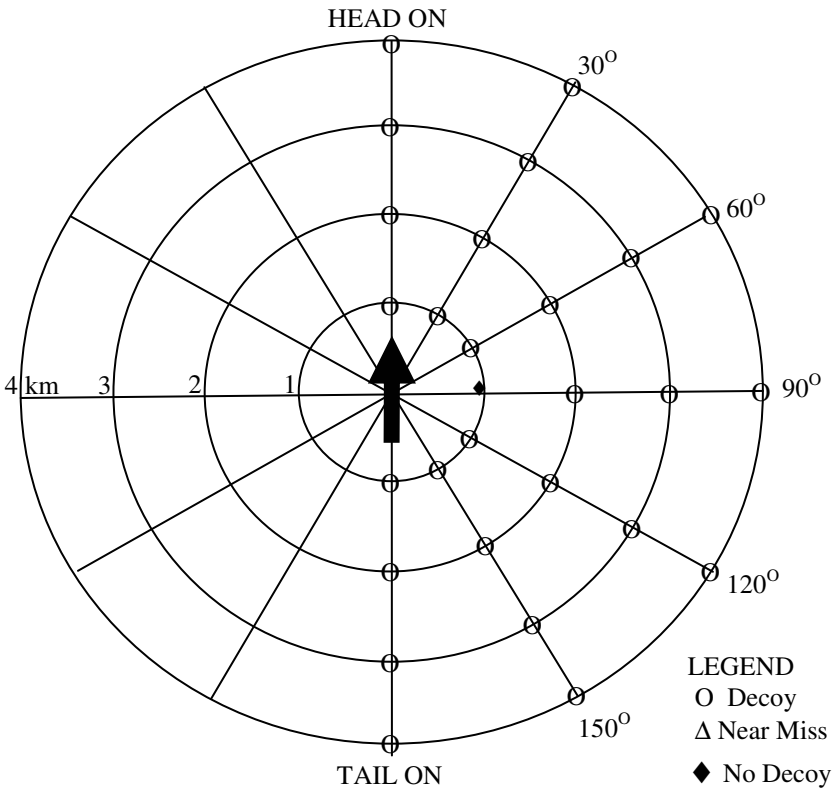

Figure 9-47 : Fast jet deploying aerodynamic flare C_D 1.0 in different directions

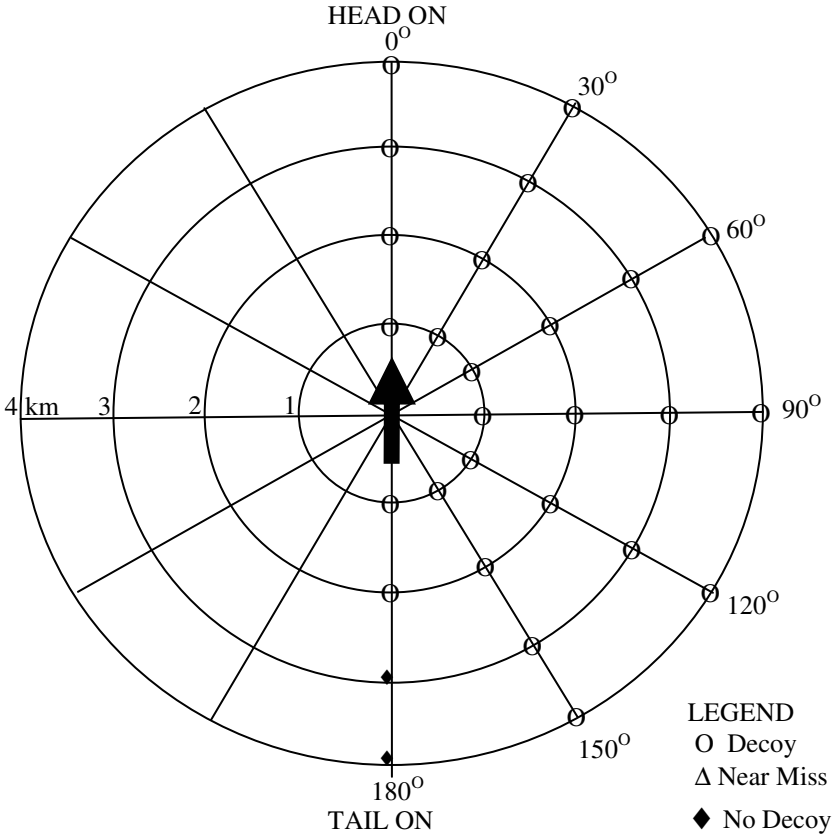

Figure 9-48 : Fast jet deploying aerodynamic flare C_D 0.1 fired in different directions

9.10.2.1 Discussion on the Results of the Initial IRCM Analysis

Comparing the CounterSim results, shown in the Figure 9-44 of the fast-jet deploying standard flare fired downward, with my simulation results shown in Figure 9-46 for the same scenario, reveals poor matching. The CounterSim simulation results show that the self-protection level is about 20% due to 10 "Decoy" points out of total 49 data points. Most of the data points on beam aspect or crossing targets were "No Decoy" points. Whereas, my simulation results shows that in most of the cases the flare has successfully countered the missile, a successful "Decoy" and the self-protection level is about 89%. The three "No decoy" points for a beam aspect at 1 km range are mainly because once dispensed at short ranges the flare rapidly moves out of the seeker FOV before being detected by the missile seeker. The self-protection level for the aerodynamic flare in my simulation is even higher, as shown in Table 9-14.

Table 9-14 : Summary of simulation results of fast jet deploying flare

FLARE	C_D	Downward	-45 pitch	Forward
STANDARD	2.4	89% miss	89% miss	89% miss
AERODYNAMIC	1.0	96% miss*	96% miss*	96% miss*
AERODYNAMIC	0.1	93% miss**	93% miss**	89% miss***

NOTE: * 1 pts at 1km beam hit due to flare out of FOV at start.
** 2 pts tail 3- 4km relock (t>3.5sec) 78% in 3-5 micron
*** 2pts same as above + 1 pt at 1km relock (t<3.5sec)

The most probable reason for this mismatch is a lack of a kinematic CCM feature in my seeker model. Because of this, irrespective of the separation rate, the flare is always effective and provides about 89% protection even with the standard flare fired downward. Also, in CounterSim at the time of launching, the missile was pointing directly towards the target, whereas, in my algorithm at launch, the missile was looking horizontally in the negative Z-direction and after launch the missile was turning under the LATAX limit towards the target aircraft. Also the feature of launching the missile from any aspect between head-on to tail-chase with 30 deg steps was not available and was implemented in the algorithm later on. Another difference between the CounterSim and my simulator is the missile guidance course. In CounterSim, the missile follows a Proportional Navigational (PN) intercept course with a maximum lead-angle of 17 degree for fast crossing targets [RIC06]. Whereas, in my simulator the missile follows a Pursuit course guidance which does not need any lead-angle and steers directly towards the target at all times. Due to these

differences between CounterSim and my simulator, the results of the initial IRCM analysis could not be used for validation. Therefore, to overcome these limitations as discussed above, a few improvements in the target manoeuvrability and missile tracking algorithm are made. These changes are explained in the following paragraphs.

9.10.3 Adding Kinematic CCM Module in Seeker Algorithm

Once the standard flare is deployed to deceive heat-seeking missile, the flare quickly separates from aircraft due to the considerable aerodynamic drag. This fast separation is used as a cue by the seeker to discriminate between the real and false target. Initially, the kinematic CCM seeker was not incorporated in the algorithm. However, to model modern missile seekers, this feature is considered and later on incorporated in the algorithm as the missile CCM module. To incorporate the kinematic CCM technique, the seeker is forward biased once the flare separation rate is more than the reference input separation rate. For this purpose, the X-component of the centroids (X_{cent}) calculated by the binary-centroid tracker is constantly monitored for the presence of two or more centroids in the FOV of the seeker. Before being detected by the missile seeker the flare travels some distance behind and below the aircraft. The separation of the flare from the aircraft along the X-axis (X_{diff}) may be calculated using Equation 9-3 as the difference between the maximum and minimum centroid values within the FOV.

$$X_{diff} = \max(X_{cent}) - \min(X_{cent}) \qquad \textbf{(9-3)}$$

The X_{diff} is compared with the reference maximum separation (sep_{max}) which is based on the angular separation (θ_{sep}) being fed in as an input parameter. As the X_{diff} is given in number of pixels so the θ_{sep} is also converted into a corresponding number of pixels using Equation 9-4 which is derived from the triangles shown in Figure 9-49.

$$sep_{\max} = \tfrac{1}{2} \times (No\_of\_pix) \frac{\tan(\theta_{sep})}{\tan(FOV/2)} \qquad \textbf{(9-4)}$$

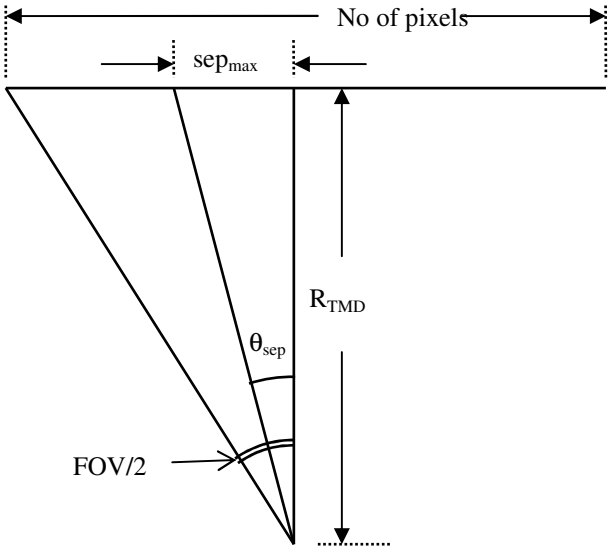

Figure 9-49 : Explaining missile CCM maximum separation

The X_{diff} is monitored for the two consecutive frames and if this remains greater than the reference maximum separation (sep_{max}) the flare is declared as a false target and the missile seeker head direction is advanced towards the aircraft in the horizontal direction. This is done by selecting the minimum binary-centroid value $min(X_{cent})$ in place of the centroid calculated by the centroid tracker

$$X_{CM} = \min(X_{cent}) \qquad \textbf{(9-5)}$$

Alternatively, if the separation in less than the reference separation the same centroid is used as calculated by the centroid tracker.

$$X_{CM} = X_{CM} \qquad \textbf{(9-6)}$$

The forward bias feature is only implemented in the horizontal direction for the cases when the missile is chasing the target aircraft from beam aspects or crossing with some angle. For the tail-chase or the head-on aspects the forward-bias is not implemented as the separation is negligible in the horizontal direction. The kinematic CCM seeker logic can easily be understood using the flowchart shown in Figure 9-50. The algorithm is implemented using "*if*", "*switch*", "*regionprops*" and "*centroids*" functions of MATLAB.

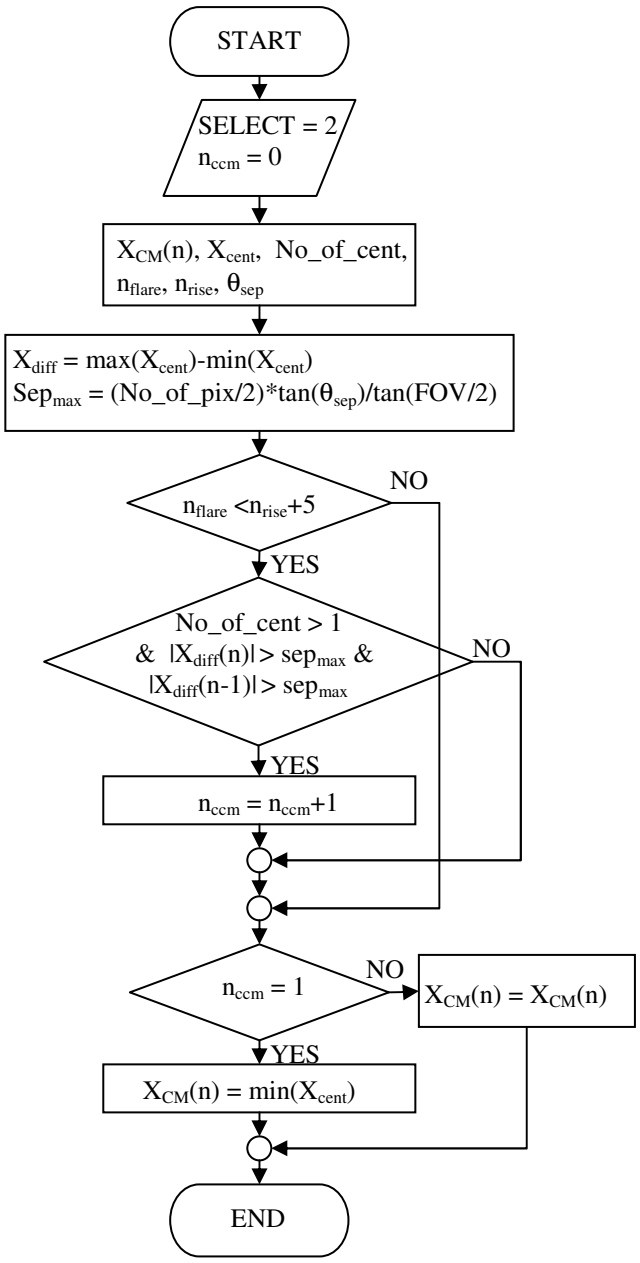

Figure 9-50 : Flow diagram explaining the missile kinematics CCM algorithm

9.10.4 Changes in Target Aircraft Manoeuvrability Algorithm

In Chapter-8 paragraph 8-8, the target aircraft manoeuvrability algorithm is discussed in detail. Figure 8-6 shows some manoeuvres which the target aircraft can perform. For the missile-target engagement simulation, the target aircraft is initially positioned at some desired location and aspect with respect to the missile. However, the aircraft could only move in head-on, tail-chase and beam aspects or crossing tangentially in beam aspect. To simulate real missile-target engagement scenarios, the algorithm

should cover launching of a missile from any aspect all around the target. To overcome this limitation the target manoeuvrability algorithm is modified. The logic used for the straight-and-level flight discussed in Chapter-8 and summarized in Table 8-4 is replaced with Equation 9-7.

$$\lfloor Z_{tgt\_loc} \quad X_{tgt\_loc} \rfloor = pol2cart(rot_{tgt\_ini}, step_{tgt} \times n) \qquad \textbf{(9-7)}$$

Where, "n" is the number of frames and $step_{tgt}$ is the target step in one frame as calculated in Equation 8-17 of Chapter-8. The rot_{tgt_ini} is the missile-target initial aspect which could be selected in steps of 30^o from zero to 180^o with zero degrees representing head-on and 180^o as tail-on. At every frame the new value of the X- and Z-component of the target location are calculated using Equation 9-7 and are then added to the target initial location X_{tgt_start} and Z_{tgt_start} respectively. The final translation field of the target aircraft is given in Equation 9-8. The Y-component is incremented by Y_{inc} as per the ROD of the aircraft for cases where the aircraft is not in the level flight.

$$myworld.tgt.translation = \begin{bmatrix} X_{tgt\_start} + X_{tgt\_loc} \\ Y_{tgt\_start} - Y_{inc} \\ Z_{tgt\_start} + Z_{tgt\_loc} \end{bmatrix} \qquad \textbf{(9-8)}$$

Similarly, in Chapter-8 Table 8-5 summarizes the logic used for the aircraft in level-turn flight. The aircraft could start either with head-on/tail-on aspects or with beam/tangential aspects as shown in Figure 8-7. The logic for the aircraft in a level-turn is now amended as per the new modes given in Table 9-15.

The initial X- and Z-components of the location of the target aircraft in a level-turn are calculated by converting the initial rotation "rot_{ini}" and the turn-radius "TR" values from polar to Cartesian coordinates as given in Equation 9-9.

$$\lfloor X_{tgt\_ini} \quad Z_{tgt\_ini} \rfloor = pol2cart(rot_{tgt\_ini}, TR) \qquad \textbf{(9-9)}$$

Table 9-15 : Modified aircraft translation and rotation fields for level-turn modes

Mode	Initial Direction	Rotation Field (Initial)	Rotation Field (0 1 0 ϕ_{tgt})	rot (initial)	rot =
Tail-on (180 deg)	- Z	(0 1 0 0^o)	+ n x ROT_{int}	0	rot - ROT_{int}
Crossing target (150 deg)	- X	(0 1 0 30^o)	- n x ROT_{int}	$5\pi/6$	rot + ROT_{int}
Crossing target (120 deg)	- X	(0 1 0 60^o)	- n x ROT_{int}	$2\pi/3$	rot + ROT_{int}
Crossing target (90 deg)	- X	(0 1 0 90^o)	- n x ROT_{int}	$\pi/2$	rot + ROT_{int}
Crossing target (60 deg)	- X	(0 1 0 120^o)	- n x ROT_{int}	$\pi/3$	rot + ROT_{int}
Crossing target (30 deg)	- X	(0 1 0 150^o)	- n x ROT_{int}	$\pi/6$	rot + ROT_{int}
Head-on (0 deg)	+Z	(0 1 0 180^o)	- n x ROT_{int}	0	rot + ROT_{int}

After finding the initial direction of the target aircraft as per the mode selected, the location of the aircraft in-turn is incremented in each frame as per the changing rotation "*rot*" and the "*TR*". Equation 9-10 gives the X- and Z-components of the aircraft location in-turn.

$$\lfloor X_{tgt\_loc} \quad Z_{tgt\_loc} \rfloor = pol2cart(rot, TR) \qquad \textbf{(9-10)}$$

The final translation field for the aircraft in level-turn modes is given by Equation 9-11

$$myworld.tgt.translation = \begin{bmatrix} X_{tgt\_start} + X_{tgt\_loc} - X_{tgt\_ini} \\ Y_{tgt\_start} - Y_{inc} \\ Z_{tgt\_start} + Z_{tgt\_loc} - Z_{tgt\_ini} \end{bmatrix} \qquad \textbf{(9-11)}$$

9.10.5 Missile Orientated to Look Directly at Target at Launch

In my algorithm the missile initial LOS (direction at launch) was always along the positive Z-axis. That means irrespective of the relative position of the target aircraft in world coordinates, the missile always starts with horizontal position and moves along the positive Z-axis. After modifying the target manoeuvrability algorithm, as mentioned in paragraph 9-10-4 above, the aircraft now can be placed initially at any aspect with respect to the missile in the horizontal plane and can move in any direction relative to the missile. Although, this may work correctly to simulate the air-to-air engagements in which the aircraft and missile are in same horizontal plane, however, in the case of a surface-to-air missile simulation, where the missile and

aircraft are not in the same horizontal plane the missile is launched in a horizontal direction but then steers up as per the altitude of the target aircraft. Ideally, to counter this limitation, the missile-LOS must be raised at launch. Presently, this feature is not incorporated in the algorithm and as an alternate to reduce the effect of the LATAX a higher value of load-factor G's is fed in to increase the LATAX to rapidly steer the missile towards the target aircraft. Although this is not a proper solution it is used for the time being and in future work the algorithm may be modified accordingly.

9.10.6 IRCM analysis with Kinematic CCM Seeker

After incorporating the requisite changes in the missile tracker algorithm for the kinematic CCM and modifying the target manoeuvrability algorithm, the same analysis carried out earlier are repeated to see the effect on the results and compare the results with CounterSim for validation. The missile-target engagement simulation is carried out for the following six setups for expendable flares to investigating the affects of standard/aerodynamic flares fired forward/downward and also the affects of aircraft manoeuvre on the missile-target engagement from different aspects. The results for the following six cases are compiled on the polar plots and are shown in Figure 9-51 to Figure 9-56 respectively.

(a) Standard flare C_D 10.0, firing backward,

(b) Standard flare C_D 10.0, firing straight forward,

(c) Standard flare C_D 10.0, firing downward,

(d) Aerodynamic flare C_D 1.0 fired forward @ -30 deg pitch,

(e) Aerodynamic flare C_D 1.0 fired forward @-30 deg pitch from aircraft in level-turn, and

(f) Aerodynamic flare C_D 0.1 fired forward @-30 pitch.

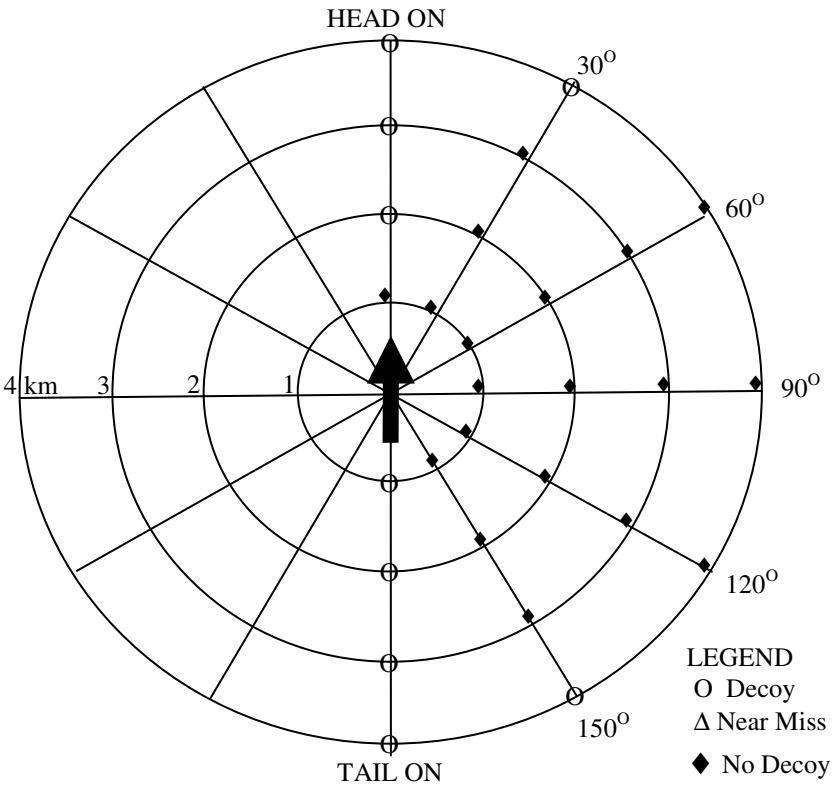

Figure 9-51 : Standard flare C_D 10.0 fired backward

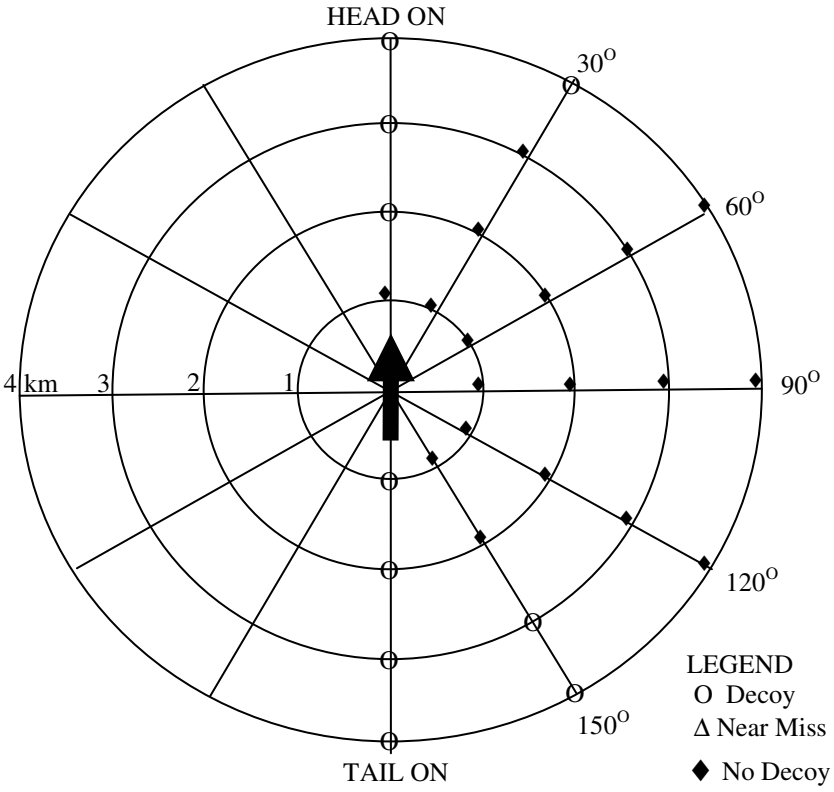

Figure 9-52 : Standard flare C_D 10.0 fired downward

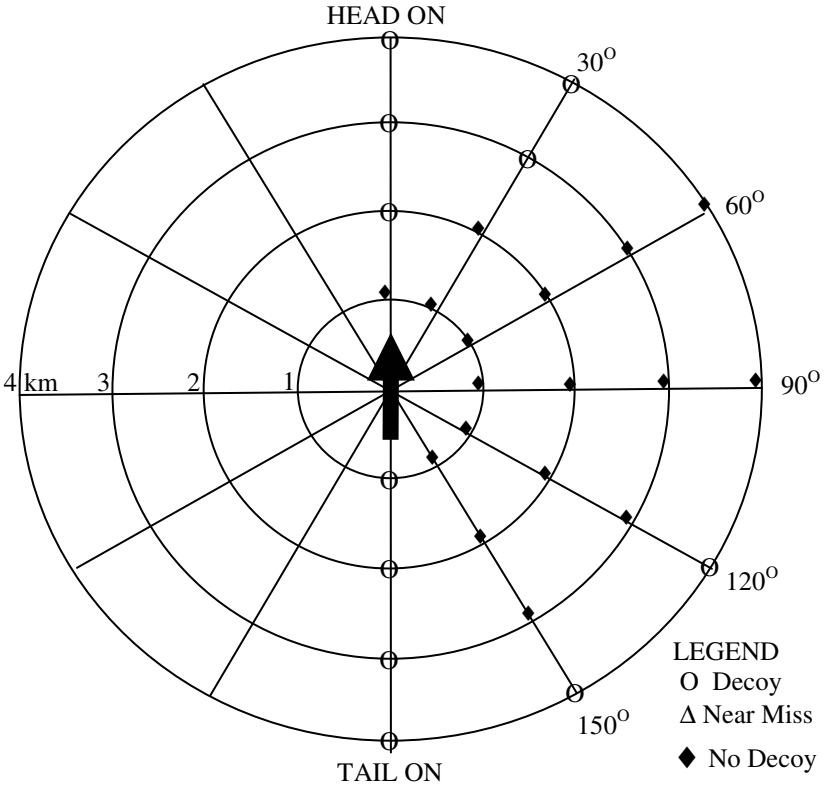

Figure 9-53 : Standard flare C_D 10.0 fired forward

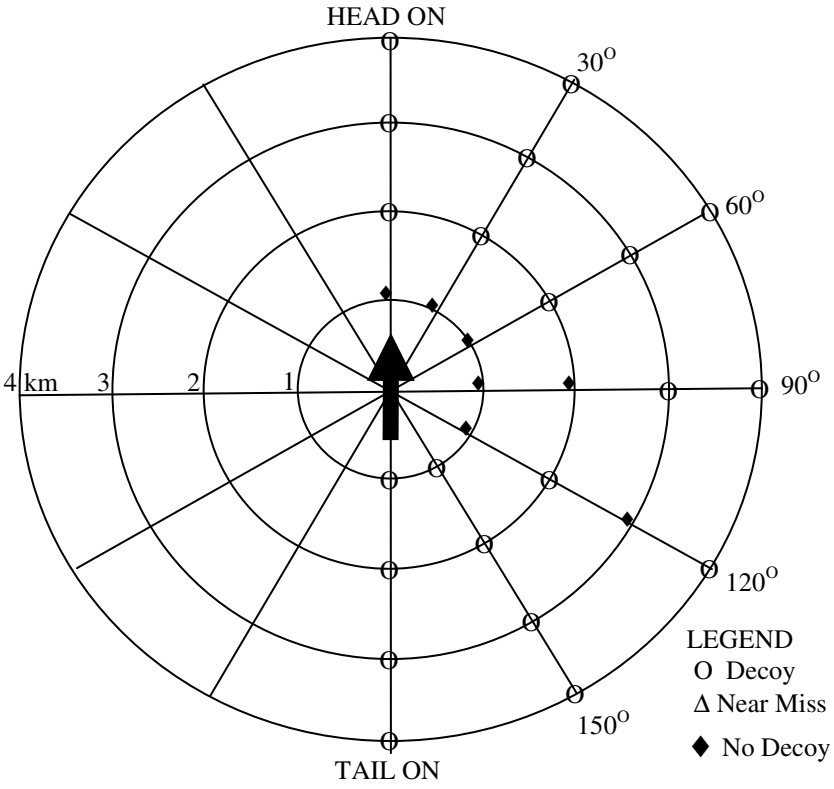

Figure 9-54 : Aerodynamic flare C_D 1.0 fired forward @ -30 deg pitch

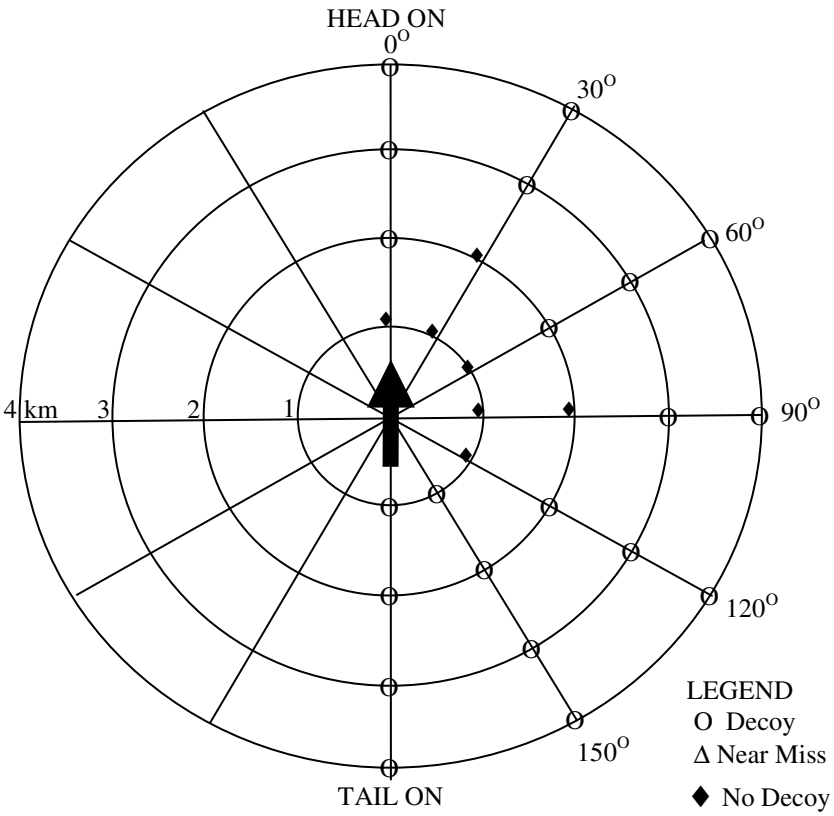

Figure 9-55 : Aerodynamic flare C_D 1 fired forward @-30 deg pitch from aircraft in-turn

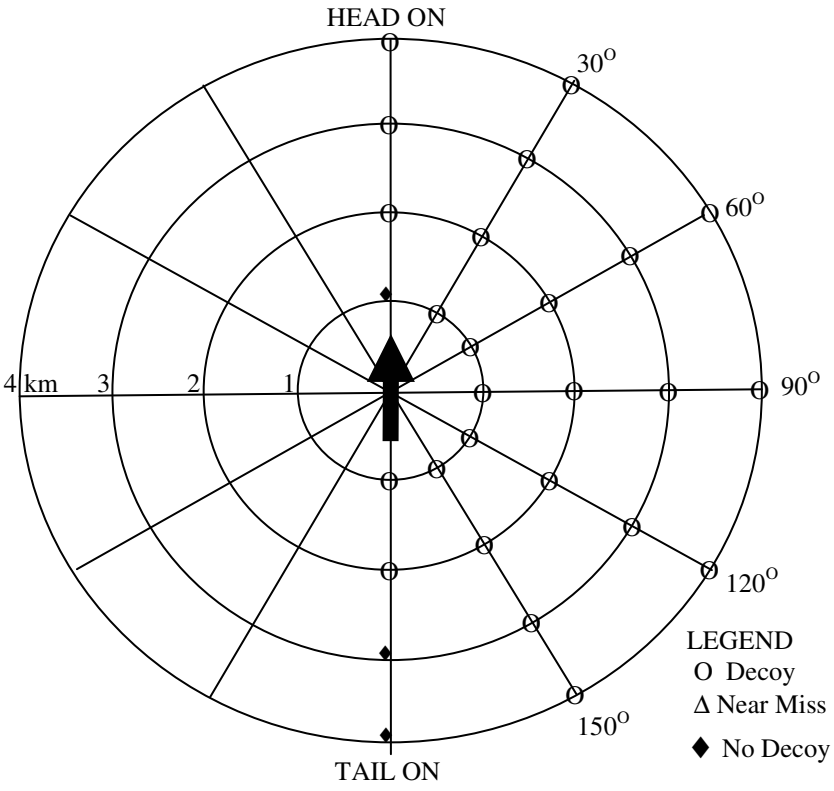

Figure 9-56 : Aerodynamic flare C_D 0.1 fired forward @ -30 deg pitch

The results for a typical fast-jet deploying a standard flare with C_D 10.0 fired backward are shown in Figure 9-51. Out of 28 data points distributed around the aircraft, the flare is reasonably effective in head-on/tail-on engagements. However, due to the addition of the kinematic CCM seeker, at lateral aspect or crossing targets, a large number of "no decoy" points are observed. Comparing the results after the kinematic CCM shown in Figure 9-52 for the standard flare fired downward with the previous analysis without kinematic CCM shown in Figure 9-46, most of the crossing target points have converted from "decoy" to "no decoy". This shows that the kinematic CCM algorithm is in-effect.

9.10.7 Discussion on Results of IRCM Analysis with Kinematic CCM

The results of the CounterSim simulations shown in Figure 9-42 to Figure 9-45 and the results of my simulations shown in Figure 9-51 to Figure 9-56 are summarized in Table 9-16. The results are shown as the self-protection level for the head-on/tail-on aspects and for the lateral aspects of 30 to 150 degree as the crossing targets. These results are analysed in the following paragraphs.

Table 9-16 : Summary of the IRCM analysis results of the CounterSim and my simulator

Type of Flare and Firing Direction	CounterSim		My Simulator	
	Head-on/ Tail-on	**Crossing Targets**	**Head-on /Tail-on**	**Crossing Targets**
Standard C_D 10.0 Fired backward	71.4% (10/14)*	5.7% (2/35)	87.5% (7/8)	10.0% (2/20)
Standard C_D 10.0 fired forward	71.4%** (10/14)	5.7% (2/35)	87.5% (7/8)	20.0% (4/20)
Standard C_D 10.0 fired downward	57.1% (8/14)	5.7% (2/35)	87.5% (7/8)	15% (3/20)
Aerodynamic C_D 1.0 fired forward @ -30 deg pitch	57.1% (8/14)	74.3% (26/35)	87.5% (7/8)	70.0% (14/20)
Aerodynamic C_D 0.1 fired forward @ -30 deg pitch	No data available	No data available	62.5% (5/8)	100% (20/20)
Aerodynamic C_D 1.0 fired forward @ -30 deg pitch level-turn	No data available	No data available	87.5% (7/8)	70.0% (14/20)

* (Decoy points / total data points)

** Self-protection level given as percentage

9.10.7.1 Fast-jet Aircraft deploying a Standard Flare Fired backward

In Table 9-16, for the case of fast-jet aircraft deploying a standard flare fired backward, the self-protection level for head-on/tail-on aspects is about 87.5% and for crossing targets is 10%. The results of the CounterSim for the same setup are as 71.4% and 5.7% respectively. Although, the results are not perfectly matching,

however, they are showing the same contrast in head-on/tail-on and crossing targets. The variations could be due to the differences in the missile guidance (Pursuit course and Proportional Navigation) and the target manoeuvrability algorithms (unable to look directly towards the target) as discussed in Paragraph 9-10-3-1 above.

9.10.7.2 Fast-jet Aircraft Deploying a Standard Flare Fired Forward/Downward

In Table 9-16, the second and third rows show the results of the fast-jet aircraft deploying a standard flare fired straight forward and downward. In my simulations, comparing with the standard flare fired backward, the level of self-protection for head-on/tail-on aspects is about the same and for crossing targets has increase to 20%. Whereas, the results of the CounterSim shows that fired forward or downward does not attribute any improvement in the self-protection level. In my simulation results, the two additional points at the 150^{o} and 120^{o}, 4 km range has been declared as "decoy" which increases the self-protection level in the crossing target case. This could be due to the fact that the kinematic CCM logic is implemented only in the horizontal direction and is not considered for variations in the vertical direction, and consequently causes wider oscillation in crossing targets at 150, 120, 60 and 30 degree aspects and may cause intermittent results at these data points.

9.10.7.3 Fast-jet Aircraft Deploying Aerodynamic Flare Fired Forward

In Table 9-16 under my simulation column, the case of a fast-jet deploying an aerodynamic flare C_D 1.0 fired forward @-30 deg pitch shows the results of the self-protection level for crossing targets as about 70%. Comparing this with the crossing target results of the CounterSim (74.3%) the self-protection level is about the same. The small difference could be attributed to the same reasons as mentioned above in the standard flare analyses.

9.10.7.4 Comparing Standard Flare with Aerodynamic Flare C_D 1.0

In Table 9-16, comparison of standard flare results with aerodynamic flare results of my simulations shows that for crossing targets the self-protection level has increased from 10% to 70% with an improvement of 60%. Whereas, in the case of CounterSim results for the same crossing targets the change was from 5.7% to 74.3% with an improvement in self-protection of 68.6%. These results are not exactly matching but

show the same trend in the improvement in the self-protection level. The variation of 8.6% could be due to the difference in the missile guidance and target manoeuvrability algorithms as discussed above.

9.10.7.5 Comparing Standard Flare with Aerodynamic Flare C_D 0.1

Figure 9-56 shows the results of the aerodynamic flare with C_D 0.1 fired forward @-30 deg pitch. Comparing the results, given in Table 9-16 under my simulator column, for an aerodynamic flare C_D 0.1 with a standard flare fired backward in head-on/tail-on aspects, the self-protection level has decreased from 87.5% to 62.5%. This could be because of the reason that in tail-on aspects the target aircraft and the flare remains within the seeker FOV for a greater time (> t_{burn}) and causes the missile to re-lock the target after flare burn out. However, in the crossing target cases the flare has shown a great improvement of 90% protection as compared to the 10% protection of a standard flare fired backward. These results could not be validated as no data was available from CounterSim simulations for the aerodynamic flare with C_D 0.1. The validation of these results may be done in further work.

9.10.7.6 Fast-jet Aircraft Deploying Aerodynamic Flare while In-turn

In Table 9-16 comparing the results of the fast-jet aircraft performing manoeuvres along with dispensing aerodynamic flare with aircraft dispensing aerodynamic flare in straight and level flight revealed that the self-protection level has remained unchanged at 87.5% and 70% in head-on/tail-on and crossing-targets respectively. Typically, it was expected that the self-protection level will increase as the aircraft manoeuvres along with dispensing flares. However, the result produced here seems unrealistic and needs to be investigated further with aircraft taking evasive manoeuvres or climbing up or down. These results could not be validated as the available results form the CounterSim simulations are only for the aircraft flying in straight-and-level flight.

9.11 Summary

The results of the IR signature modelling, the missile-target engagement and flare deployment are analysed and some are validated against the published results. Four separate test scenarios are used to generate the results. The effects of the temperature, emissivity and atmospheric attenuation on the IR radiations are analysed. The power received at the detector is analysed in the 3-5 and 8-12 micron wavebands. The effect

of the target cross-sectional area, temperature and range are analysed on the lock-on range. The output of the imaging seeker is analysed as the 256x256 pixel images in the 3-5 and 8-12 micron wavebands. The appearance of the IR signatures of high-fidelity sub-targets are analysed using different colour-maps. The material properties of VRML are investigated to model the special effects such as the exhaust-gas plume, leading-edges and the cold-sky reflections from the glass canopy. The missile lateral acceleration is analysed for different speed and load-factors during missile-target engagement simulations. The missile control algorithm is accounting for the missile LATAX. The target location estimator algorithm is working with binary and centroid trackers. The IR flare spectral response is analysed in 3-5 and 8-12 micron wavebands. The flare temporal response is analysed for the burn-time and the rise-time. The effects of the drag coefficient, mass of the pallet and the firing angle on the flare ballistic trajectory are analysed and the results are validated against published data. The IRCM analysis is performed for several flare types and firing angles. The kinematic CCM module is incorporated in the missile seeker algorithm and the target manoeuvrability algorithm is modified to simulate crossing target engagements. The analysis and results are validated against published results of the CounterSim simulator.